The representation of the Pacific/North American pattern and North Atlantic Oscillation in the Canadian Seasonal to Interannual Prediction System, and their association with surface air temperature and various flow features

Nicholas Soulard

Degree of Master of Science

Department of Atmospheric and Oceanic Sciences

McGill University

Montreal, Quebec, Canada

August 2014

A thesis submitted to McGill University in partial fulfillment of the requirements of the degree of Master of Science

©Nicholas Soulard, 2014

Abstract

We use Singular Value Decomposition to statistically correct the winter seasonal-mean geopotential height field of the Canadian Seasonal to Interannual Prediction System (CanSIPS). This process aims to correct model errors associated with the three leading patterns of Tropical Pacific sea-surface temperature anomalies. This process, due to the already present skill of the models, is unable to improve the forecasts. The PNA is seen to be predictable up to a year ahead of time, while significant skill is found for the NAO out to the one-month lead forecast. We then examine the reasons behind the forecast skill observed for the PNA, and possible predictability sources for each the PNA and NAO.

We examine the association of the PNA and NAO with the near-surface air temperature, skin temperature, and the temporally decomposed 500 hPa geopotential height field. This association is examined via correlation of these field variables with the PNA and NAO indices, calculated by projecting the geopotential height anomalies onto rotated empirical orthogonal function loading patterns.

Our results show that the PNA's link to the Tropical Pacific Ocean is predictable out to a nine-month lead forecast, due to the models' significant skill in forecasting the temperature in this region. The NAO's relationship to this same region is seen to be slightly nonlinear in the reanalysis data, but not captured by the models. Both teleconnection patterns have predictability sources in the Eurasian temperature. The temperature pattern associated with the NAO is present in local areas of high correlation in Eastern China, and the Himalayas, but missing over Western Europe. Due to similarities in the model correlation maps, and a lack of correlation in the

reanalysis data, it is impossible to determine if this region plays a role in the predictability of the PNA in the models. Finally the tri-pole pattern in the Atlantic sea-surface temperature in association with the NAO is well represented in the models in seasons following an NAO event, but not prior.

The geopotential height field is decomposed into low-frequency eddies (10-90 day periods) and synoptic transients (two-nine day periods) using a Fourier time filter. The 90 day variance is then averaged over a 32 year period. The main features in both frequency bands are fairly well reproduced by the models, both in terms of the relative importance of each feature on the map and location. The low-frequency eddy field depicts two variance maxima; one over the Aleutian Islands which is slightly too strong compared to the maximum over Iceland. The centre over Iceland is displaced to the southeast, which is manifested again in the synoptic transients by a similar shift in the storm track. Furthermore the temperature patterns associated with the PNA and NAO are visible in the models with the exception of a lack of significant skill over Western Europe.

Finally we examine the use of a 31-point digital filter with Lanczos smoothing, which represents a simpler, computationally less expensive alternative to the Fourier filter.

Résumé

Nous avons utilisé la décomposition en valeurs singulières pour corriger la hauteur géopotentielle moyenne pour l'hiver, téléchargé de la Canadian Seasonal to Interannual Prediction System (CanSIPS). Ce processus vise à corriger les erreurs des modèles informatiques associées aux trois patrons principaux reliés à la température de la surface de l`océan Pacifique tropical. Ce processus, en raison de la compétence déjà notée des modèles informatiques, n'a pas amélioré les prévisions. Le PNA s'est avéré prévisible jusqu'à un an à l'avance. Un bon niveau de compétence a été trouvé pour la NAO dans les prévisions d'un mois d'avance. Nous avons ensuite examiné les raisons pour la bonne performance observée dans les prévisions de la PNA, et les sources de prévisibilité possibles pour le PNA et le NAO.

Nous avons aussi examiné l'association du PNA et de la NAO avec la température de l'air près de la surface, la température de la surface de l`océan, et la hauteur géopotentielle de la surface 500 hPa temporellement décomposée. Cette association est examinée par corrélation de ces variables aux indices du PNA et NAO, calculée en projetant les anomalies de la hauteur géopotentielle sur les patrons PNA et NAO.

Nos résultats montrent que le lien entre le PNA et l'océan Pacifique tropical est prévisible jusqu`à neuf mois d`avance, en raison du bon niveau de compétence des modèles informatiques à prévoir la température dans cette région. Le lien entre la NAO et cette même région est considérée comme légèrement non-linéaires dans les données réanalysées, mais pas capturé par les modèles informatiques. Les deux modèles de téléconnexion ont des sources de prévisibilité reliées à la température Eurasienne. Le patron de température associé à la NAO est présent dans des zones locales de forte corrélation en Chine de l'Est, et dans les montagnes de l`Himalaya,

mais absent sur l'Europe occidentale. À cause des similarités dans les cartes de corrélation, et une absence de corrélation dans les données réanalysées, il est impossible de déterminer si cette région joue un rôle dans la prévisibilité du PNA. Finalement, le tri-pôle dans la température de surface de l'Atlantique, en association avec la NAO, est bien représenté dans les modèles informatiques dans les saisons qui suivent un événement NAO, mais pas dans celles qui précèdent.

Le champ de hauteur géopotentielle est décomposé en tourbillons de basse fréquence (périodes de 10-90 jours) et transitoires synoptiques (périodes deux-neuf jours) en utilisant un filtre temporel Fourier. La moyenne de la variance de 90 jours est ensuite calculée sur une période de 32 ans. Les caractéristiques principales dans les deux bandes de fréquences sont bien reproduites par les modèles informatiques, à la fois en termes de l'importance relative de chaque entité sur la carte et de l'emplacement. Il y a deux maxima de la variance dans le champ des tourbillons à basse fréquence; un sur les îles Aléoutiennes qui est trop fort par rapport au maximum près de l'Islande. Le centre près de l'Islande est déplacé vers le sud-est et se manifeste à nouveau dans les transitoires synoptiques par un changement similaire dans la trajectoire des tempêtes. En outre, les patrons de la température associée aux PNA et NAO sont visibles dans les modèles informatiques à l'exception d'un manque de compétence sur l'Europe occidentale.

Enfin, nous avons examiné l'utilisation d'un filtre numérique de 31 points avec lissage Lanczos. Ceci représente une alternative plus simple, moins coûteuse en calcul qu`un filtre de Fourier.

Acknowledgements

I would like to take this opportunity to thank my co-supervisor Dr. Hai Lin. His guidance, and support throughout my thesis have made this whole process more instructive and rewarding than I ever would have imagined! He was always willing to help with coding, discuss results, and answer any questions I had. I would also like to thank my co-supervisor Dr. Jacques Derome for his advice and moral support; especially before my first ever seminar! Furthermore I would like to thank both of my supervisors for their comments and feedback on the first version of this thesis.

I am eternally grateful for the financial support provided to me by Dr. Lin, which permitted me to focus all of my energies on my research, and allowed me to attend this year's CMOS conference, which was the highlight of my time at McGill. I would like to thank the entire Atmospheric Science department at McGill. Every professor and student alike was always very helpful and friendly, making these past two years so enjoyable.

Finally I would like to express my heartfelt gratitude to all of my friends and loved ones for their support and encouragement.

Table of Contents

Abstract i
Résumé iii
Acknowledgements v
Table of Contents vi
List of Figures viii
List of Tables x
1 Introduction 1
2 Data and Methodology 7
2.1 Data 7
2.2 Methodology 11
2.2.1 Climate Means and Standard Deviations 11
2.2.2 Skill Score 12
2.2.3 Singular Value Decomposition (SVD) 14
2.2.4 Time Filtering 16
3 The Mean Seasonal State and Results of SVD Analysis 20
3.1 Preface 20
3.2 Mean Winter Atmospheric State 21
3.3 The Leading SVD Patterns 25
3.4 Correction of Model Bias using SVD 29
4 Predictability Sources of the Teleconnection Patterns 34
4.1 Link to ENSO 34
4.1.1 PNA 34
4.1.1 NAO 39
4.2 The North Atlantic Ocean's Relationship to the NAO 42
4.3 Eurasian Temperature and Snow Depth 47
4.3.1 NAO 47
4.3.2 PNA 54
5 High- and Low-Frequency Eddies 56
5.1 Representation of Low-Frequency Eddies 56

5.2 Representation of the Synoptic Transients 61
5.3 A Brief Comparison between the Fourier and Digital Filters 66
6 Conclusion 69
7 References 75

List of Figures

Figure 1.1: PNA and NAO patterns. 4

Figure 2.1: Various scatter plots depicting correlations 13

Figure 2.2: Frequency response of 31 point Lanczos filter (Hoskins et al. 1983) 18

Figure 3.1: 500 hPa geopotential height mean winter and standard deviation. 22

Figure 3.2: 500 hPa height bias 23

Figure 3.3: Skin temperature field bias. 24

Figure 3.4: Standard deviation of DJF skin temperature. 24

Figure 3.5: The leading two SVD patterns for 500 hPa geopotential height and SST. 26

Figure 3.6: One-month lead forecast multi-model SVD modes 1 and 4. 27

Figure 3.7: Forecast skill before correction and after correction. 30

Figure 4.1: Skill of 9-month lead DJF Multi-Model SST 35

Figure 4.2: Regression of PNA index onto surface temperature. 35

Figure 4.3: Forecast skill of the Nino-3.4 index for all forecast lead times.. 37

Figure 4.4: PNA index plotted against the Nino-3.4 index 39

Figure 4.5: NAO index versus Nino-3.4 index 40

Figure 4.6: Regression of SST anomalies onto the NAO index.. 43

Figure 4.7: Regression of SST anomalies 500 hPa height PCs. 43

Figure 4.8: First Atlantic SVD reanalysis and multi-model modes. 44

Figure 4.9: Regression of first Atlantic 500 hPa height PC onto skin temperature 46

Figure 4.10: Simultaneous correlation of near-surface air temperature with the NAO index. 47

Figure 4.11: Correlation of SON WEASD and Nov. 2m Temp. with the DJF NAO index. 52

Figure 4.12 : As in Figure 4.11 with the DJF PNA index. 55

Figure 5.1: 32-year averaged 10-90 day variance of 500 hPa height 57

Figure 5.2: As is Figure 5.1 but normalized by the maximum value on the map 60

Figure 5.3: Low-frequency 500 hPa height and 2m air temp. forecast skill 60

Figure 5.4: 32 year average of normalized 500 hPa height two-nine day variance 62

Figure 5.5:Two-nine day variance bias. 62

Figure 5.6: Correlation of two-nine day transients NAO, PNA, and Nino-3.4 indices. 64

Figure 5.7: Forecast skill of high-frequency 500 hPa geopotential height and 2m air temp. 65

Figure 5.8: As in Figure 5.1 but for the digital filtered two-nine day variance climate. 67

Figure 5.9: As in Figure 5.1, but for the digital filtered data. 67

Figure 5.10: As in Figure 5.5 but for the digital filter 10-90 day eddies. 68

Figure 5.11: As in Figure 5.7 but for the synoptic transients. 68

Figure 5.12: As in Figure 5.4 (left panel) for the Tropics, using the digital filter 68

List of Tables

Table 2.1: NCEP/NCAR variable list with associated reliability category. 10

Table 3.1: Correlation between each PC time series and the PNA and NAO indices.. 27

Table 3.2: Skill of original and "corrected" multi-model PNA and NAO indices. 30

Table 3.3: Percent of the squared covariance explained by each pair of DJF SVD patterns..... 31

Table 3.4: Correlation of PNA and NAO indices for various correction procedures……33

Table 4.1: Correlation between Nino-3.4 Index and PNA index..... 37

Table 4.2: PNA and NAO indices correlated with Nino-3.4 index for various ENSO phases..... 40

Table 4.3: Correlation of PCs from both SVD analyses with the NAO index. 45

Table 4.4: Correlation of Snow Depth Index with the Temperature index. 50

Table 4.5: Correlation of Eurasian Indices with DJF NAO index. 51

1 Introduction

The atmosphere is an inherently chaotic system. Producing an accurate forecast of the daily weather therefore depends on numerous factors such as: the model used, the state of the atmosphere prescribed as initial conditions, and the boundary conditions, to name only a few. Meteorological observations cannot span the entire globe, or a continuous time span; they are discrete by definition. For perfect initial conditions to be input into a model, we would require data for every point on the globe, and in time, as well as equipment with no measurement error. Practically speaking it is impossible to obtain complete data coverage over the globe, and all measurements contain some uncertainty associated with the instrument used. In light of this, no matter how accurate the initial conditions there will always be some error present in predictions by even the most advanced models. A small error in the initial conditions of a model will grow in time to produce a completely different atmospheric state than observed. Because of this it is generally accepted that the skillful prediction of day-to-day weather patterns extends out to approximately two weeks (Lorenz 1969).

One way to avoid the aforementioned limitations is to concern ourselves with the time-mean state of the atmosphere, rather than the instantaneous state. Shukla (1981) showed that most of the inter-annual variability in the 500 hPa geopotential height field is accounted for by large scale, low-frequency (10-90 day periods) anomalies, and that these fluctuations are predictable more than a month in advance. In recent decades, there has been a growing interest in the predictability of the mean-seasonal state of the atmosphere. Daily weather patterns have life times of roughly 2-10 days; computing a time-average over a season effectively filters out these

high-frequency variations (the weather). The seasonal mean then becomes less dependent on processes internal to the atmosphere, and more dependent on external forces, or boundary conditions. Some such external forces are variations in sea-surface temperature (SST), snow-cover, and sea ice, which vary on much longer time scales due to their high thermal and mechanical inertia. Thus it would be reasonable to assume that the predictability of low-frequency atmospheric fluctuations would be associated with these boundary forcings.

Using seasonal averages does not remove all of the high-frequency variability present in the models. Even though the unpredictable high-frequency fluctuations are mostly filtered out by the seasonal and ensemble averaging (averaging over many forecasts), there is still some error present. The differing formulation of the models introduces another source of error; each model will force the atmosphere in somewhat different ways given the same boundary forcing. These errors can be partially corrected by applying singular value decomposition (SVD) (Bretherton et al. 1992), and following the methods of Lin et al. (2005) (to be described in more detail in Section 2.2.3). SVD finds coupled patterns of variability between observed two fields such as the tropical Pacific SST and the northern hemisphere 500 hPa geopotential height field. These patterns then provide a basis to correct the models' biases (Feddersen et al. 1999; Lin et al. 2005).

Variations in sea-surface temperature can be skillfully predicted as much as a year in advance in the tropical Pacific Ocean (Latif et al. 1994). This result would then imply that any atmospheric circulation anomalies associated with the SST variations in this region would also have an extended range of predictability, perhaps even surpassing one month. These SST anomalies can affect the atmospheric state over the globe via teleconnections (Wallace and Gutzler 1981). Of particular importance are the SST anomalies in the tropical Pacific Ocean,

which are correlated with the geopotential height fields over much of North America. As a result, there have been numerous studies aimed at understanding the nature of this relationship (e.g. Horel and Wallace (1981); Mo et al. (1998); Pozo-Vázquez et al. (2005)). SST anomalies tend to persist for long periods of time (up to several months) due to the high thermal and mechanical inertia of water. The SST anomaly is then transmitted to the air above it via sensible and latent heat release, acting as a thermal forcing. Since the thermal and mechanical inertia of the air is so much lower than that of the ocean, the SST anomaly acts as a slowly-varying boundary forcing to the atmosphere. The relationship between the tropical Pacific SST and the Northern Hemisphere geopotential height field is well documented, and provides a source of potential predictability for large-scale flow patterns in the atmosphere.

Of the teleconnections patterns described by Wallace and Gutzler (1981), the two most important patterns for the wintertime extra-tropical Northern Hemisphere are the North Atlantic Oscillation (NAO) and the Pacific-North American (PNA) pattern (Barnston and Livezey 1987) (Figure 1.1). These two patterns account for the highest proportions of the total temporal variance in the geopotential height field and directly affect the weather over much of the Northern Hemisphere. The PNA has been shown to be the dominant mode of atmospheric variability related to anomalies in the tropical Pacific SST (Horel and Wallace 1981). Due to the significant correlation skill of the SST anomalies one would expect a similarly significant skill for the PNA. On the other hand, there is much less evidence that the NAO is linked to an external forcing (Hurrell et al. 2003), leading to many studies attempting to find some such link. Cohen and Entekhabi (1999) suggested that fall snow-cover anomalies over Europe and Asia affect the Northern Hemisphere circulation by exciting a pressure pattern resembling the NAO, and numerous studies have been conducted that support this finding. There have also been

studies linking variation in the NAO to anomalies in the Atlantic Ocean (Lin and Derome 2003; Peng et al. 2003), and to ENSO (Derome et al. 2005; Pozo-Vázquez et al. 2005).

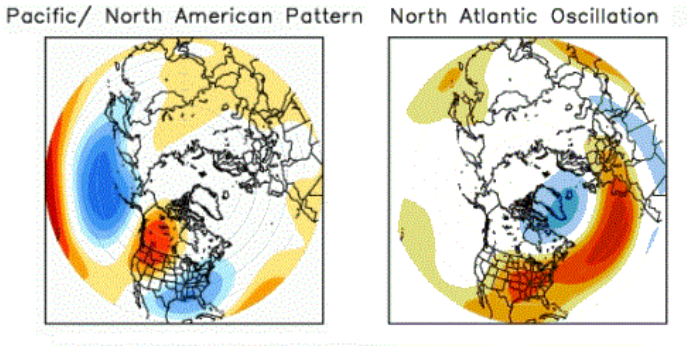

Figure 1.1: PNA and NAO patterns. (Images taken from www.cpc.ncep.noaa.gov/data/teledoc/pna_map.shtml; and www.cpc.ncep.noaa.gov/data/teledoc/nao_map.shtml)

Many previous studies have used atmospheric general circulation models (GCMs) to examine the relationship between the SST and the Northern Hemisphere height field. For these models, the climatological SST is computed and perturbed by the anomalies from the previous month, which are then persisted for the remainder of the forecast period. For forecasts of a few months or less, this persistence method has proved sufficient; however, for forecasts that extend further than a few months a coupled atmosphere-ocean model would be necessary.

For the purposes of this project, the forecast system used is the Canadian Seasonal to Interannual Prediction System (CanSIPS), which is the operational seasonal forecast system used at Environment Canada. CanSIPS consists of two global atmosphere-ocean coupled models, CanCM3 and CanCM4. Starting from the beginning of each month, a year-long integration is carried out producing 10-member ensemble forecasts per model. Here, each ensemble member is produced by initializing the models with different initial conditions. Each ensemble member is therefore a forecast of the atmospheric conditions, so that when all members are taken into account a spread of possible atmospheric conditions is obtained. Using the ensembles to compute

an ensemble average will reduce the models' sensitivity to the initial conditions. In addition the ensemble average forecasts have been shown to improve predictability when compared to any of the individual members (Murphy 1988). For the reasons listed above, the present study will only make use of ensemble averages unless otherwise indicated.

One such instance will be in the computations of the variabilities of the synoptic transients and low-frequency eddies, which consist of anomalies with two-nine day, and 10-90 day periods, respectively. Many studies examine the predictability of seasonally averaged quantities; however, there are relatively few which attempt to quantify the models' skill in reproducing the amount and intensity of temporally decomposed fields over a season. The variance of the high-frequency transients provides insight into the amount and intensity of extreme events, while that of the low-frequency eddies gives some indication as to the intensity and duration of variabilities with longer lifetimes.

In a fashion similar to the predictability study conducted for the PNA and NAO, the locations, amplitudes, and inter-annual variability of the temporally decomposed field will be examined. The locations of the low-frequency eddies in the 500 hPa geopotential height fields are in good agreement with the locations of the standing waves (Blackmon 1976). In the same study, the two-nine day eddies were associated with shorter waves associated with the two major storm tracks off the east coasts of Asia and North America, just north of 40^{o}. Here storm tracks refer to the locations where the two-nine day transients exhibit their maximum amplitude. In other words, they are the most frequent paths followed by alternating high and low pressure systems. Thus the accurate prediction of these features directly affects the forecasts over the Northern Hemisphere.

To summarize, the main objectives of this study are to determine whether the CanSIPS system adequately represents various atmospheric flow features ranging in time scale from synoptic transients, to seasonal teleconnection patterns, to determine the signal sources responsible for the predictability of the PNA and NAO patterns, and to examine whether the association between these teleconnection patterns, and other variables (such as near-surface air temperature) and flow features (such as storm tracks) are also realistically captured. As will be described in Chapter 2, the CanSIPS models store a year-long integration beginning at the beginning of *each* calendar month. The majority of this study makes use of the November initialized forecasts for the December-February (DJF) season (one-month lead).

A description of the models and data sets, as well as the analysis methods will be outlined in Chapter 2. The mean-seasonal state of the atmosphere and the results of the Singular Value Decomposition analysis and statistical forecast correction will be described in Chapter 3. The predictability sources for the PNA and NAO will be described in Chapter 4, while the representation of the temporally decomposed fields and their association to the teleconnection patterns will be outlined in Chapter 5. Chapter 6 will contain a brief summary and some concluding remarks.

2 Data and Methodology

2.1Data

This study uses the Canadian Seasonal to Interannual Prediction System (CanSIPS), which consists of two global atmosphere-ocean coupled models (CanCM3 and CanCM4). CanSIPS is currently the operational seasonal forecasting system at Environment Canada. The data used are the historical forecasts (hindcasts) from the Coupled Historical Forecast Project, phase 2 (CHFP2), based at the Canadian Center for Climate Modelling and Analysis (CCCma) at Environment Canada, for the period of January 1979 to November 2011. Both daily averages and monthly averages are available online, and used in this study.

CanCM3 and CanCM4 are both composed of an atmospheric and oceanic model component. While they share the same ocean model, CCCma's fourth-generation ocean model (CanOM4), they differ in their atmospheric components. CanCM3 uses the CCCma's third-generation general circulation model (CanAM3, or AGCM3). CanAM3 uses a T63 horizontal resolution, 31 sigma pressure levels which extend from the surface to 1 hPa. CanCM4's atmospheric component is CanAM4, which has the same horizontal resolution as CanAM3 but has 35 vertical levels over the same pressure range as CanAM3, allowing for better coverage over the troposphere. CanAM4 also includes many upgraded physical parameterizations. Both models use the same land-surface processes scheme, represented by the Canadian Land Surface Scheme (CLASS) version 3, and sea-ice dynamics are represented in both models according to the cavitating fluid approach.

The atmospheric and oceanic model components communicate with each other once per day. Simply put, the atmospheric component passes daily averaged heat and momentum fluxes to the ocean component, which then steps forward in time and passes the new SST back to the atmosphere for the new day. CanCM3 and CanCM4 predictions are each composed of 10 ensemble realisations. Instead of using initial conditions from ten different points in time prior to the initialization time, perturbed initial conditions are used, whereby each ensemble member is initialised using slightly differing conditions to represent the possible spread of atmospheric conditions which arise from the uncertainty present in any initial condition. For more information on the model formulation and initialization, please refer to Merryfield et al. (2013).

All atmospheric data are re-gridded to 2.5x2.5 degrees, with 5 vertical levels (850 hPa, 500 hPa, 200 hPa, 100 hPa, and 50 hPa) for the three-dimensional fields. While this resolution is too coarse to resolve features on a regional scale, it is sufficient to resolve the larger scale flow features, such as those mentioned in the previous chapter. As mentioned above, the hindcasts are initialized at the beginning of each month from January 1979 until December 2010, and are each one year in duration, thus providing 7680 years (2 models x 12 integrations/model x 10 members/integration x 32 years) of monthly and daily averaged data available for analysis.

Of all the atmospheric, ocean, and sea-ice fields, this study focuses on only a handful of the atmospheric variables. The 500 hPa geopotential height is used to calculate teleconnection indices, and general circulation patterns. Skin temperature, which is defined as SST over the sea, soil temperature over land, and ice temperature over ice, is primarily used to capture SST anomalies. Near-surface air temperature, thickness of surface snow amount in metres of water equivalent (WEASD), mean sea-level pressure, top of the atmosphere outgoing longwave radiation, and precipitation rate, are used to either verify that the response to various

teleconnection patterns are well reproduced, or to examine possible sources of predictability of these same patterns. For comparison the National Centers for Environmental Protection/National Center for Atmospheric Research (NCEP/NCAR) reanalysis datasets are used.

The NCEP/NCAR reanalysis dataset is composed of a frozen global data assimilation system to provide a constant and consistent set of reanalysis products. All of the aforementioned variables are also available in the reanalysis set from January 1948 until the present. This allows for all 32 of the model years to be compared with the corresponding NCEP/NCAR datasets. One caveat, however, is the fact that these products are reanalysis and not observations. Observational data, as well as model data, are taken into account when producing any reanalysis product. Each variable in the reanalysis dataset is either strongly or weakly influenced by their observations, and their modelled counterparts. For example geopotential height fields over land are strongly influenced by the observations, and only weakly by the model data, whereas the outgoing longwave radiation at the top of the atmosphere is strongly influenced by the model output and not influenced by the observations. All reanalysis products are categorized based on the relative influence of the observational data and the model on the final product: A, being strongly influenced by observations; B, where both the observational data and model contribute more or less equally; C, in which there is no input from observations, but the fields are forced to remain close to the atmosphere by the data assimilation process; and finally D represents a field fixed to its climatological value. Therefore variables that fall into category A can be viewed as reliable, while variables in categories B and C should be treated carefully. For a list of the variables examined and their categories refer to Table 1. For a complete description and listing of the NCEP/NCAR reanalysis dataset refer to Kalnay et al. (1996).

NCEP/NCAR Variable	Category
Geopotential height	A
Near surface (2m) air temperature	B
Skin temperature	B
Water equivalent of surface snow thickness	C

Table 2.1: NCEP/NCAR variable list with associated reliability category.

Many of the relationships presented herein were first documented using the NCEP/NCAR datasets (e.g. Wu and Hsieh 2004; Cohen et al. 2001). However in some cases (such as those mentioned above) variables from the NCEP/NCAR reanalysis dataset were compared against variables from other datasets to form the relationship, or the data was first checked against observational data. This is the case with many of the other sources cited as well. Agreement between these various datasets and the NCEP/NCAR reanalysis lends credence to the relationships documented in the following chapters. Furthermore, whenever the reanalysis data field used was of category C (e.g. water equivalent of accumulated snow depth), a related proxy variable of category B (e.g. 2m air temperature) was used to verify the relationship. In this way, some uncertainty was mitigated by agreement between both data fields. Conversely if the field from the more reliable category does not produce the relationship, any sort of comparison with the models then becomes impossible (e.g. section 4.3.2).

2.2Methodology

2.2.1 Climate Means and Standard Deviations

Given a time series, calculating the mean and standard deviation is straightforward, but still provides very important information. All equations (with the exception of 2.1) will refer to seasonal means, unless otherwise indicated.

$$x_i = \frac{1}{m}\sum_{j=1}^{m} x_j \tag{2.1}$$

$$\bar{x} = \frac{1}{N}\sum_{i=1}^{N} x_i \quad . \tag{2.2}$$

Here x_j denotes a value at month j, where m is the number of months included in the seasonal average, x_i. For these seasonal averages we define $\bar{x}$ as the climate mean, taken over all available years, N. The climate mean of, for example, the 500 hPa geopotential height field over a season, will show the locations and amplitudes of the standing waves in the atmosphere.

The standard deviation (equation 2.3) provides a measure of the inter-annual variability. Continuing with the previous example, while these standing waves are ever present in the atmosphere, their amplitude, and location may differ from year-to-year. The standard deviation depicts regions where these changes occur.

$$\sigma_x = \sqrt{\frac{1}{N-1}\sum_{i=1}^{N}(x_i - \bar{x})^2} \quad . \tag{2.3}$$

The variance will give the exact same pattern, since the standard deviation is the square root of the variance. Only the magnitude of the values will change, not the spatial pattern. The advantage of using standard deviation is that it is in units identical to the variable being analyzed, and corresponds to a representative year-to-year amplitude change at a given location. Equations (2.2) and (2.3) form the basis for many of the statistical quantities to be used later in this study.

2.2.2 Skill Score

All comparisons between the model data and reanalysis data are conducted using the correlation coefficient. Given two time series, say x_i and y_i, where i is the index corresponding to a given year, the correlation coefficient will provide a quantitative measure of the linear relationship between the two. It is calculated as follows:

$$r_{xy} = \frac{\sum_{i=1}^{N}(x_i - \bar{x})(y_i - \bar{y})}{\sigma_x \sigma_y} \quad . \tag{2.4}$$

Where x_i and y_i will be replaced with model and/or reanalysis fields, their corresponding climatological averages and standard deviations as calculated from equations (2.2) and (2.3).

One thing to keep in mind throughout these analyses is the fact that the correlation coefficient provides a measure of the linear relation between two variables. Thus even if a nonlinear relationship exists this statistic will not detect it (Figure 2.1). That is not to say

however, that if a nonlinear relationship does exist that the correlation coefficient will give a result of 0; in fact this will occur in the case when the data are spread symmetrically (i.e. high values of y are associated with both high and low values of x, or vice versa).

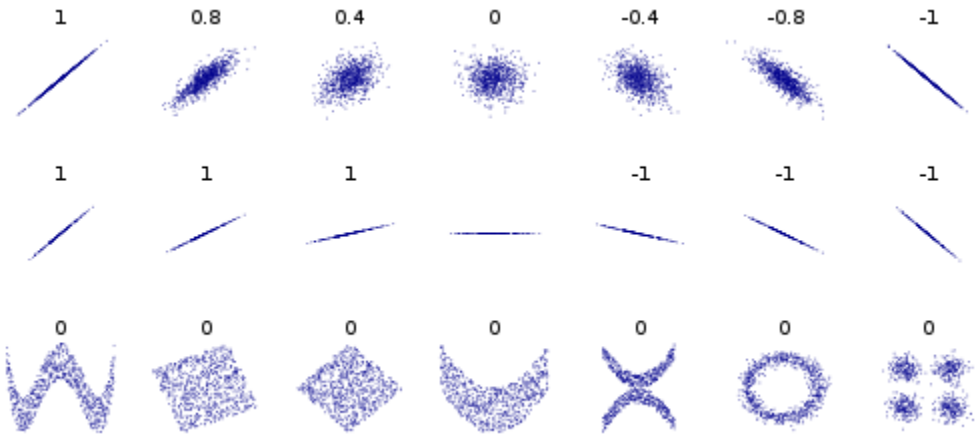

Figure 2.1: Various scatter plots depicting the relationship between the correlation coefficient and the spread of the points about an arbitrary line (top row) and the slope of the line (middle row). The bottom row illustrates that while a relationship may exist, if it is not linear this statistic may not detect it.

For the purposes of this study, the time series at each grid point for the model data and reanalysis data are compared to generate correlation maps. This will be done in two ways: simultaneous correlation, and lagged correlation. Simultaneous correlation refers to both times series being taken from the same season, while in lagged correlation one of the two time series are from a month, or season, preceding the other. Simultaneous correlation allows for the direct comparison of the same field from two different sources (e.g. model vs. reanalysis) determining how well one represents the other. It can also be used between two different fields from the same source to verify and quantify the relationship between these two fields. Simultaneous correlation reveals nothing about the cause/effect relationship, whereas lagged correlation can give some indication of a possible relationship, since one field precedes the other in time.

2.2.3 Singular Value Decomposition (SVD)

Singular value decomposition is a statistical method for finding time-correlated pairs of spatial patterns from the covariance matrix of two variables (Bretherton et al. 1992). Each pair of patterns contains are associated with each of the respective covariates used to calculate the covariance matrix. Furthermore the pairs of patterns are ordered based on the amount of squared temporal covariance they explain in descending order. The first pair of patterns therefore represents the patterns explaining the highest proportion of the total squared temporal covariance. The time evolution of these pairs of patterns can be obtained by projecting the original data field for each covariate onto the respective spatial patterns in each pair. In this way the each pattern in the pair can vary in its own time. These time series, known as principal components (PCs), can be used to statistically correct model forecasts by creating a linear regression model using the first few PCs from the model data and the corresponding reanalysis data field (Lin et al. 2005).

The statistical correction is done by using a subset of the PCs of the variable of interest from the model data, which account for the majority of the total squared temporal covariance, and the corresponding reanalysis data field. The following section provides a general procedure for the calculation of the PCs, and correction process, given that the SVD patterns have already been derived. For a detailed description of the calculations involved refer to Bretherton et al. (1992). Let the SVD patterns be denoted by *SVD[i x k]*, where *i* is the number of grid points on the map, and *k* is the number of patterns used for the "correction" process. In other words, for a given *k*, *SVD[i x k]* represents pattern *k*. Finally, let *X[i x t]* denote the model data anomaly

(deviation from the time mean) field for *i* grid points and *t* times, then the calculation of the PCs is as follows:

$$PC[t\ x\ k] = X[i\ x\ t]^T SVD[i\ x\ k] \tag{2.5}$$

These PCs thus show how these SVD patterns evolve in time. They are then used as the basis of a linear regression model in conjunction with the reanalysis field. Now let $Z[i\ x\ t]$ be the reanalysis counterpart to $X[i\ x\ t]$, and $Z_n[i\ x\ t]$ denote the "new" corrected forecasts.

$$Z_n[i\ x\ t] = \hat{\beta}[k\ x\ i]^T PC[t\ x\ k]^T \tag{2.6}$$

where $\hat{\beta}[k\ x\ i]$ are the regression coefficients defined as:

$$\hat{\beta} = ([PC^T PC]^{-1} PC^T) Z^T \tag{2.7}$$

In the training of the linear regression model, the year for which the regression coefficients are being calculated is omitted. This cross-validation approach ensures that the predicted data is independent from the training data, and also avoids over-fitting the training data to the model.

The use of the reanalysis data in calculating the regression coefficients is what removes the systematic bias. Since the models and reanalysis do not produce the exact same SVD patterns, the reanalysis patterns are used as the basis. The new forecasts adopt the same spatial structures as those in the reanalysis data set; however, they vary in time according to the PCs of their own corresponding structures. In addition to statistically removing model biases to improve forecasts, simply examining the structure and temporal variability of the coupled patterns provides some insight into how the models behave.

2.2.4 Time Filtering

In this section two different time filtering techniques will be described: time filtering using Fourier transforms, and using a digital filter. Each has its own set of advantages and drawbacks. The Fourier filter has a very precise separation of periods into the high and low frequency fields, whereas a digital filter will have a transition range between the two (to be described in more detail in the following sections). Based on the above statement, one might question the advantage of using a digital filter. The advantage lies in its computational cost, which is significantly less than the Fourier filter. In this section both methods will be described, both in terms of their advantages and drawbacks, and their mathematical formulation.

2.2.4.1 Fourier Filter

The Fourier Transform is a powerful tool with many applications. For this study, it is used to spectrally decompose the time series of a data field at each point on the grid. Each time series is split into two, one part which contains fluctuations with periods from two to nine days, and another which contains fluctuations with periods ranging between 10 and 90 days. Unlike the previous mathematical tools, this one requires the use of daily data instead of the monthly data. The daily data is necessary for this decomposition because only waves which are greater than half of the sampling rate can be resolved (Hamming 1989). Put simply, using daily data it is possible to resolve waves with periods of two days or more, while using monthly data, only periods with time scales equal to or greater than two months would be resolvable. In contrast to this lower period bound, the highest resolvable period is the total duration of the time series. Only the winter months (December-February) are examined, meaning that these methods will be able to resolve variabilities with periods between two and 90 days.

In general a Fourier transform will convert a function into frequency space, where the function can be approximated as a finite sum of sine and cosine functions. These functions are weighted by coefficients which are themselves sums of sine and cosine functions. This is computed over a finite number of frequencies which are representative of the variability of the function in question and limited by the upper and lower bounds mentioned above. Presented below is an outline for filtering data at one grid point using Fourier transforms.

$$a_K = \sum_{I=1}^{N_t} Z_I * cos\left(\frac{2\pi * K * (I-1)}{N_t}\right) \quad for\ K = f_L\ to\ f_U \tag{2.8}$$

$$b_K = \sum_{I=1}^{N_t} Z_I * sin\left(\frac{2\pi * K * (I-1)}{N_t}\right) \quad for\ K = f_L\ to\ f_U \tag{2.9}$$

$$\hat{Z}(I) = \sum_{K=f_L}^{f_U} \left[\frac{2a_K}{N_t} * \cos\left(\frac{2\pi * K * (I-1)}{N_t}\right) + \frac{2b_K}{N_t} * \sin\left(\frac{2\pi * K * (I-1)}{N_t}\right)\right] \tag{2.10}$$

$$for\ I = 1\ to\ N_t$$

Equations (2.8) and (2.9) compute what are known as Fourier coefficients; where *K* is the number of periods that occur over the time interval (period number), and *I* is the number of time points. f_L and f_U denote the desired lower and upper period number bounds respectively, while N_t is the total number of time points. Using these equations to filter data one would simply calculate the Fourier coefficients for all desired periods over the entire time period, and substitute them into equation (2.10) to obtain the filtered value ($\hat{Z}$) at that point in space and time. Only the 90 days of winter will be examined, and filtered into two frequency regimes: synoptic transients (two-nine day periods) and low-frequency eddies (10-90 day periods); and so in the context of the above equations N_t would be 90, f_L would be 10 (1), and f_U would be 45 (9) for the high (low) frequency category.

2.2.4.2 Digital Filter

A digital filter is essentially a weighted running mean where the weights are chosen to pass, or block, a given set of frequencies. Instead of having a distinct cut-off, like the Fourier filter, this type of filter has a transition zone in the vicinity of this cut-off frequency (Figure 2.2). The presence of the transition zone means that there will be some high-frequency contamination in the low-frequency eddies, and vice versa. The advantage of this type of filter lies in its simplicity; unlike the Fourier filter, which must calculate the coefficients for each grid point, a digital filter has only one set of coefficients, which are then applied to the time series over the entire grid.

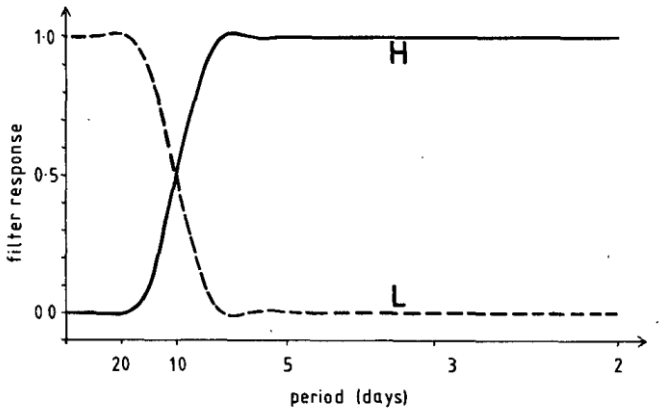

Figure 2.2: Frequency response of 31 point Lanczos filter, with frequency cut-off at 10 days. H denotes the high frequency filter response, and L the low frequency filter response. (Hoskins et al. 1983)

The filter to be used in this study is the same as that used by Hoskins et al. (1983) (Figure 2.2; their Figure B1), which uses a 31-point digital filter (n=15) with Lanczos smoothing. This smoothing process introduces a scaling factor, called the sigma factor, to reduce the Gibbs phenomenon (oscillations near the cut-off frequency which may increase the maximum amplitude of the partial sum to above the amplitude of the function being reproduced). The

frequency response function that is being reproduced is a square wave; allowing certain frequencies to pass unhindered, while completely blocking the rest. The low frequency filter has the form:

$$R(f) = \begin{cases} 1, & 0 < |f| < 0.1 \\ 0, & 0.1 < |f| < 0.5 \end{cases} \tag{2.11}$$

$$\widehat{Z_I} = \sum_{K=-n}^{n} c_K Z_{I-K} \tag{2.12}$$

where R(f) is the desired frequency response function, and all other notation is consistent with the previous section. This function can be approximated using a Fourier series, for which the coefficients can be directly calculated since this function is relatively simple. This particular response function is composed solely of cosine waves, since it crosses the "y-axis" at 1; therefore the coefficients and corresponding weights are calculated as follows:

$$a_K = 4\int_0^{0.1} cos(2\pi K f)df = \frac{2}{\pi K} sin(2\pi K * 0.1) \; \forall \; K \tag{2.13}$$

$$\sigma(n+1, K) = \frac{sin(\pi K/(n+1))}{\pi K/(n+1)} \tag{2.14}$$

$$c_K = \frac{a_K \sigma(n+1, K)}{2} \qquad for \; K \neq 0 \qquad . \tag{2.15}$$

Note that at K=0 the factor of 2 in the denominator is ignored, and a_K = 0.4. The high frequency filter is then derived from the low frequency one by setting $c_K^h = -c_K^L$, for |K|>1, where the h and L superscripts denote the high- and low-frequency filter coefficients respectively. For K=0 $c_K^h = 1-c_K^L$. These coefficients, once calculated do not change and can be applied to all points in time and space as weights to a simple 31 day running mean.

3 The Mean Seasonal State and Results of SVD Analysis

3.1 Preface

As outlined in Chapter 2, SVD patterns are used both in the context of verifying the response of the extra-tropical Northern Hemispheric 500 hPa geopotential height field to tropical SST anomalies, and statistically correcting the model forecasts by removing the systematic bias and climate noise. These results will be presented in Chapters 3.3 and 3.4 respectively.

The SVD analysis is conducted between the Northern Hemisphere 500 hPa geopotential height and the tropical Pacific SST for the model and the reanalysis data sets separately; the latter being used for comparison and verification purposes. Previous studies have linked ENSO related tropical Pacific SST anomalies to the generation of a PNA-like pattern in the atmosphere (Horel and Wallace 1981), and thus higher predictive skill for the seasonal forecasts over North America. There have also been studies linking atmospheric forcing in the tropics to the NAO (e.g. Lin et al. 2002; Greatbatch et al. 2003). These studies provide some indication of what to expect from the SVD analysis.

3.2 Mean Winter Atmospheric State

The mean seasonal state of the atmosphere, as well as the inter-annual variability is described herein. This type of basic examination provides insight into how well the models represent the mean state of the atmosphere (Figure 3.1). The mean and standard deviation of the one-moth lead forecast of the 500 hPa height field over the northern hemisphere depict the locations, as well as the average inter-annual variations of the standing troughs and ridges. The structures of the troughs in the Pacific and Atlantic basins are reproduced with very little noticeable differences when compared to the reanalysis plots (Figure 3.1). Also evident are the ridges dues to the major mountain ranges; one over the Rocky Mountains, and a weaker one over the Himalayas and Tibetan Plateau. The differences are subtle but noticeable; there is a southward shift of the Pacific trough in the models, which is reflected in the inter-annual variability; comparing the lower panels of Figure 3.1 we notice that the centre of maximum variability is displaced to the south in the multi-model average. Furthermore, the amplitude of the variability is lower, and less "noisy" in the models. This can be attributed to the ensemble averaging, which while providing improved predictability (Murphy 1988), also diminishes the internal variability through the averaging process. These differences can be better represented by taking a simple difference: the climate from the multi-model average minus that of the reanalysis (Figure 3.2). This systematic bias is what the SVD analysis corrects for; however, the standard deviation, which is lower in the models, will not be increased by this "correction" process.

By inspection Figure 3.2 shows that the locations with the highest bias coincide with the locations of the standing troughs and ridges. While the differences between the top panels in Figure 3.1 are difficult to assess, Figure 3.2 provides a much clearer view of the biases. The bias in the north Pacific coincides exactly with the location of the trough, while the one in the north

Atlantic is to the southeast of the trough. The Pacific trough is deeper in the multi-model average, which is reflected here, whereas in the Atlantic there is little bias down the centre of the trough. The larger bias values occur where the isopleths diverge; which is too far to the East in the models. This may have an effect on the location of the storm track. Given that these biases occur for different reasons, we may expect that they will have different implications for the predictability study. Furthermore, notice that all of the bias is negative. The models therefore consistently reproduce stronger troughs, and weaker ridges. Of particular note is the Tibetan Plateau region over which the models do not capture the overlying ridge pattern.

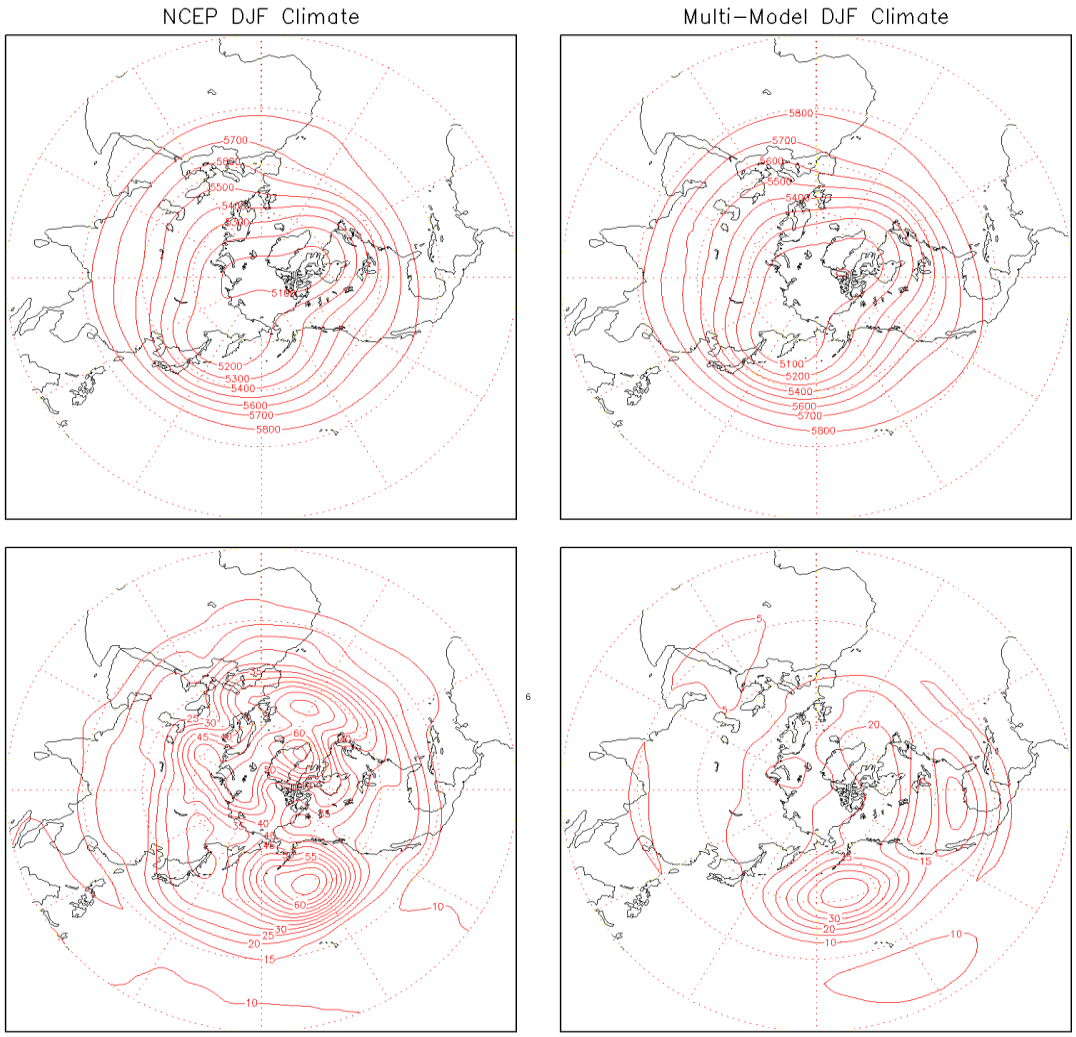

Figure 3.1: 500 hPa geopotential height mean winter (DJF) state (top panels), and standard deviation (lower panels).

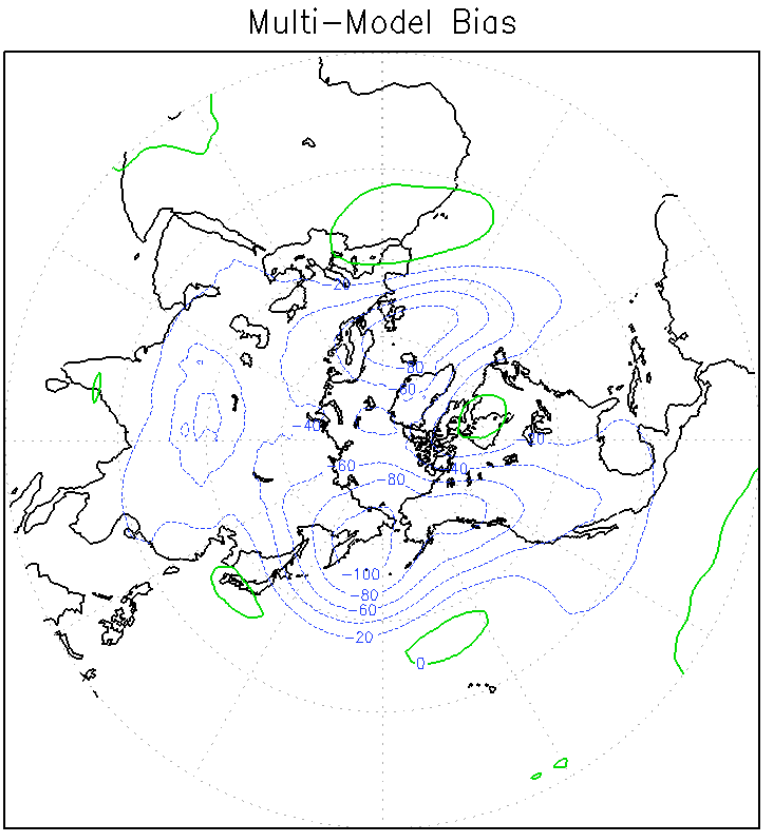

Figure 3.2: 500 hPa height multi-model climate minus reanalysis climate in metres.

The structure of the skin temperature climate (not shown) is very similar for both data sets. Warm oceans, cold land masses, and thermal troughs over mountain ranges. The biases lie mostly over landmasses poleward of 60°, in the Davis and Bering Straits, and in the Labrador and Greenland Seas (Figure 3.3). One exception is the Tibetan Plateau region, which is too warm in the models. These biases coincide with the locations of the biases in the 500 hPa geopotential height field. Also note that the oceans between 60°S and 60°N have very little bias (≤1°C). The inter-annual variations are also weaker in amplitude in the Tibetan Plateau region, while marginally stronger in the central and western equatorial Pacific Ocean (Figure 3.4).

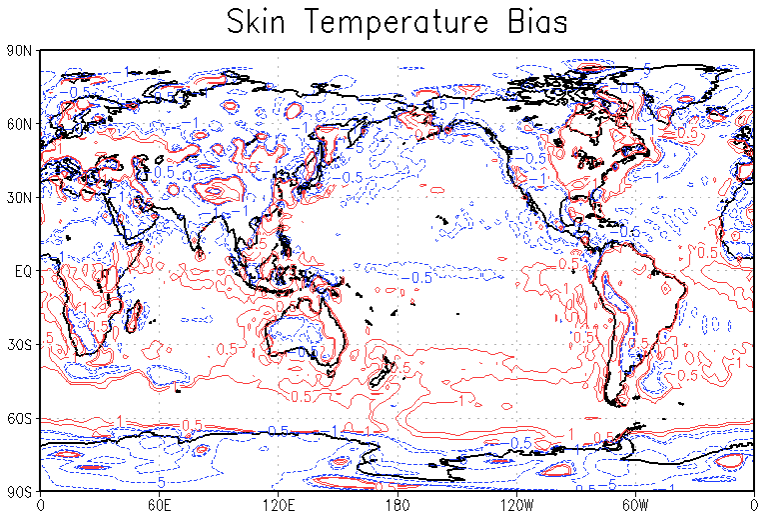

Figure 3.3: As in Figure 3.2, but for the skin temperature field. Contour levels are +(red)/-(blue) 0.5, 1, 5, 10, and 15 degrees Celsius.

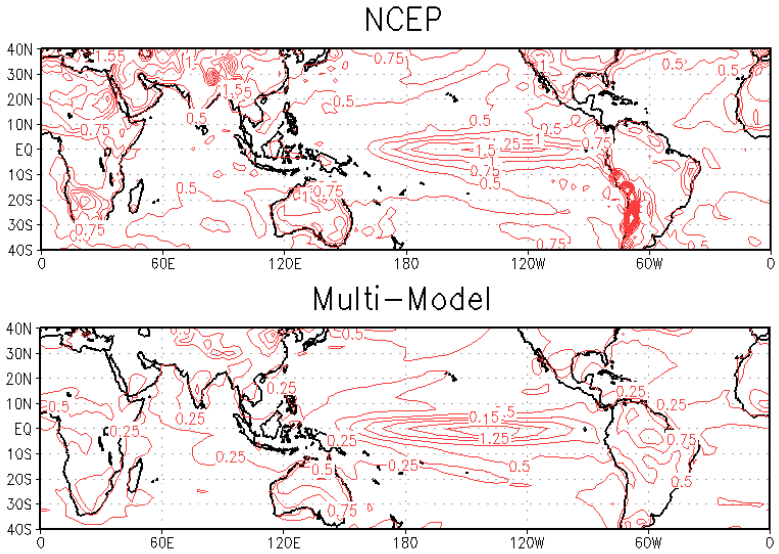

Figure 3.4: Standard deviation of DJF skin temperature.

3.3 The Leading SVD Patterns

To begin the SVD analysis only the Northern Hemisphere 500 hPa geopotential height field between 20^{o} and 85^{o} N, and the tropical Pacific SST from 40^{o} S to 40^{o} N, and 120^{o} to 270^{o} E, for the winters (DJF) of 1979/80 to 2010/11 are used. One thing to note is that even though the SVD analysis is being conducted over the exact same regions for both the one-month lead multi-model average and the reanalysis data, their SVD patterns differ. Even if this is the case, the time evolution of their patterns may be correlated. The correction process uses the reanalysis patterns for precisely this reason; having the models vary in their own time, but with the correct spatial patterns (Figure 3.5). The geopotential height patterns (top panels of Figure 3.5) resemble the Pacific/North American pattern (PNA), and North Atlantic Oscillation (NAO) described by Wallace and Gutzler (1981), and account for the highest proportions of the total squared temporal covariance between the Northern Hemisphere 500 hPa geopotential height and Tropical Pacific SST. A previous study by Barnston and Livezey (1987) lists the NAO and PNA as the two leading modes of variability in the Northern Hemisphere winter explaining the highest proportion of the total variance. Since here the PNA is the first mode explaining more squared covariance than the NAO, we expect that significant proportion of the variance of the PNA can be explained by the variability in the Tropical Pacific, while this area is of lesser importance to the NAO. The SST patterns show a positive ENSO signal associated with the positive PNA pattern (lower left panel), which agrees with previous studies (e.g. Horel and Wallace 1981; Kumar et al. 1996; Mo et al. 1998). The second SST pattern (Figure 3.5; lower right panel) shows a very weak tropical SST anomaly associated with a negative NAO pattern. This implies that the NAO is related to weak Tropical Pacific SST anomalies, while the PNA is more strongly related to the strong SST anomalies in this same area.

The same procedure for the multi-model average yields maps which are vastly different from the reanalysis maps (Figure 3.6). The first pattern resembles the PNA and accounts for over 95% of the total squared covariance, while the NAO pattern no longer appears as the second mode, but rather the fourth. This rather subjective interpretation of the patterns is supported by the PC time series of the fourth pattern which is highly correlated to the NAO index, whereas the second mode's time series is not (Table 3.1). Furthermore, unlike mode 3, which is even more strongly correlated to the NAO index, both the 500 hPa geopotential height and SST patterns of mode 4 resemble that of the reanalysis most closely.

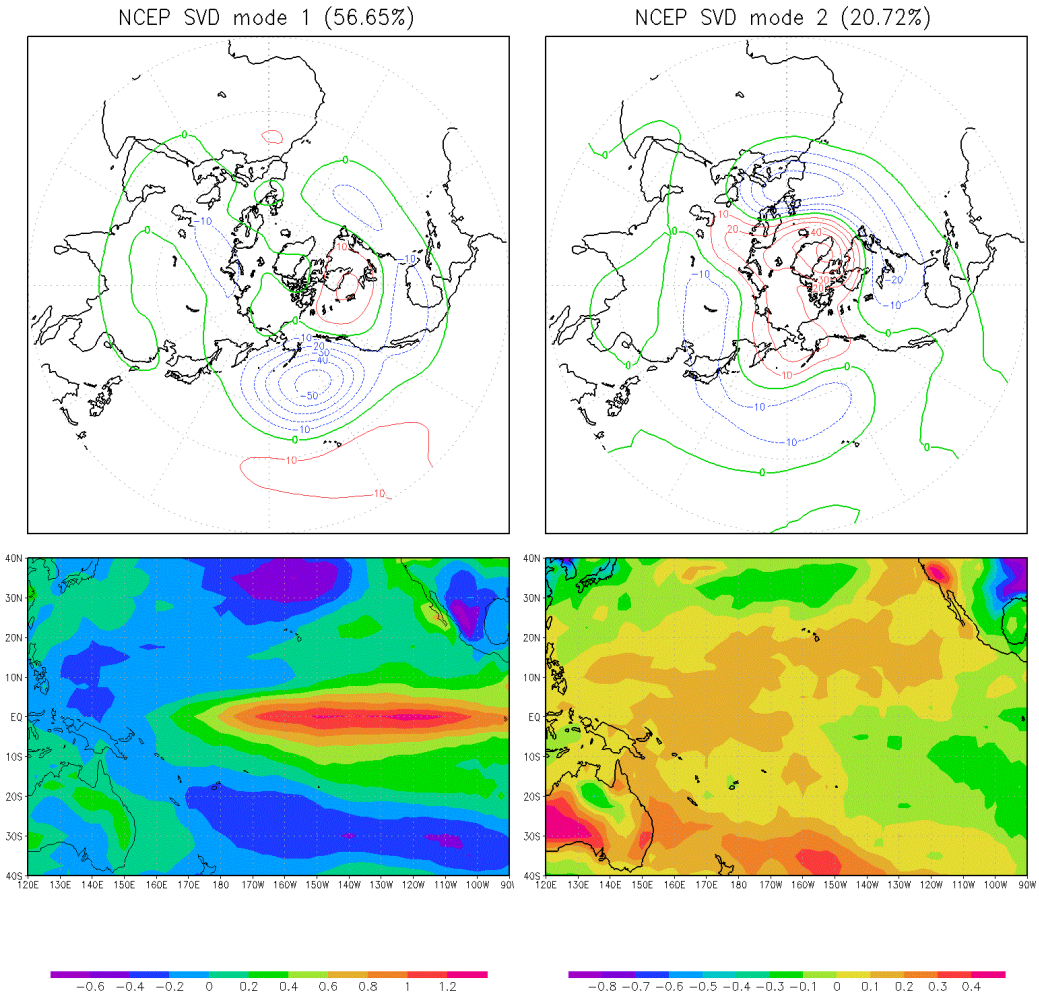

Figure 3.5: The leading two SVD patterns for 500 hPa geopotential height (upper panels), and SST (lower panels). The magnitude corresponds to one standard deviation of the PC. The value in parentheses is the percent of squared covariance explained by each pattern.

Correlation Coefficient	PC Mode 1		PC Mode 2		PC Mode 3		PC Mode 4	
	NCEP/ NCAR	Multi-Model	NCEP/ NCAR	Multi-Model	NCEP/ NCAR	Multi-Model	NCEP/ NCAR	Multi-Model
PNA	***0.81***	***0.55***	0.02	0.16	***0.36***	0.04	-0.30	0.20
NAO	-0.23	-0.24	***0.95***	0.07	***-0.38***	***-0.46***	0.02	***0.41***

Table 3.1: Correlation between each PC time series and the PNA and NAO indices. The values in bold italics pass the 95% confidence level as determined by the Student's t-test.

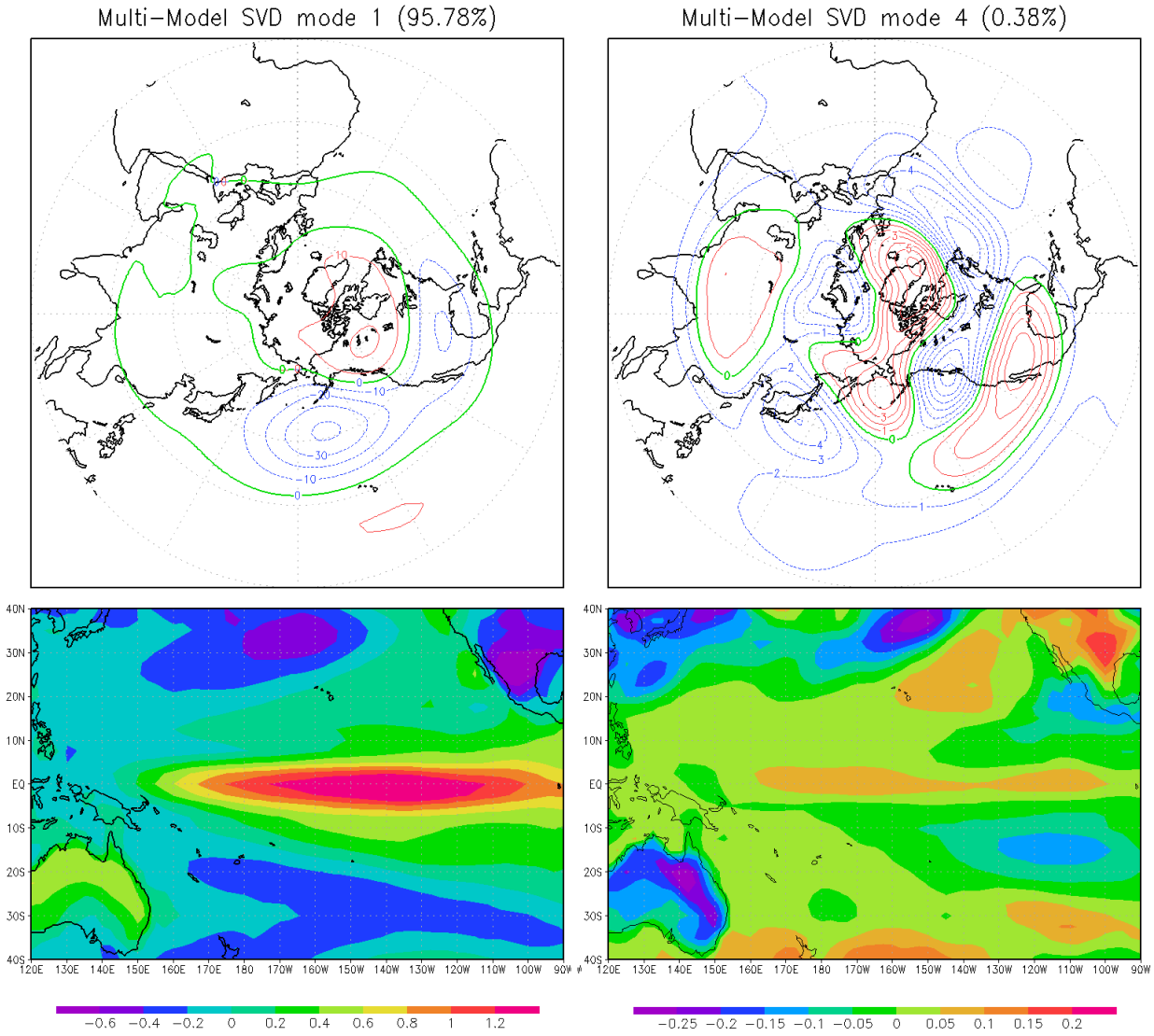

Figure 3.6: Same as in Figure 3.5, except for the one-month lead forecast multi-model SVD modes 1 and 4.

Modes 3 and 4 from the reanalysis data resemble modes 2 and 3 from the multi-model average respectively (not shown). Mode 3 of the reanalysis data is characterized by a wave train extending from the Pacific Ocean over northern Canada, to the Atlantic, while mode 4 is characterized by a "bull's-eye" to the south-southeast of Greenland, and a pattern which is reminiscent of the Eurasian pattern of Wallace and Gutzler (1981).

From the brief introduction to the SVD patterns presented above we see that the relationship between the PNA and the Tropical Pacific SST seems to be well represented by the models, whereas the NAO variability is supressed, and thus the pattern is relegated to a less "important" mode. Furthermore the PNA-SST pair of covariance patterns accounts for over 95% of the total squared temporal covariance; a value more than 150% larger than that from the reanalysis. As previously stated, a PNA pattern can be forced by an ENSO SST anomaly, whereas the NAO is a mode of variability mainly internal to the atmosphere (Robertson 2001).

The larger proportion of explained temporal covariance of the PNA pattern in the models is likely due to the ensemble averaging, which removes much of the internal variability. Similarly the smaller proportion of explained covariance of the NAO pattern in the models may also be due in part to the ensemble averaging process. Another possible explanation is that the NAO-Tropical Pacific SST link may involve more complex (nonlinear) dynamics than the PNA-SST link, which is linear in nature (Lin and Derome 2004).

3.4 Correction of Model Bias using SVD

The model correction procedure is done via a linear regression model as outlined in Section 2.2.3. The linear regression model makes use of the PC time series of the leading three patterns from the multi-model average, and the reanalysis data field. This process does not produce the complete field, but deviations from the mean; as such the corrected forecasts have no bias. To illustrate the results of the statistical correction, plots of the 500 hPa geopotential heights will be examined. Although the correction for the near surface air temperature was also performed, the results were analogous.

To begin we examined the standard deviation of the statistically modified forecasts (not shown), and compared this to the lower panels of Figure 3.1. The centres of maximum variability are congruent with those from the reanalysis, with slightly higher variability than in the original multi-model data. While the inter-annual variability structure and amplitude improve, the forecast skill does not (Figure 3.7). Even with this statistical bias correction, the overall correlation skill has diminished, or remained the same, over the entire hemisphere. This lack of improvement can be attributed to the already reasonably good skill of the original model output, especially in the tropics and PNA region. Since the model concentrates the majority of its variability in the first mode, all other modes tend to represent roughly equal proportions of variance. Using only the leading three modes excludes modes that are as important as modes 2 and 3, and therefore may degrade the correlation skill in regions dominated by the excluded patterns. Moreover, since the pattern resembling the NAO is found in the fourth SVD mode, which is excluded from the correction process, we expect that the NAO skill may decrease.

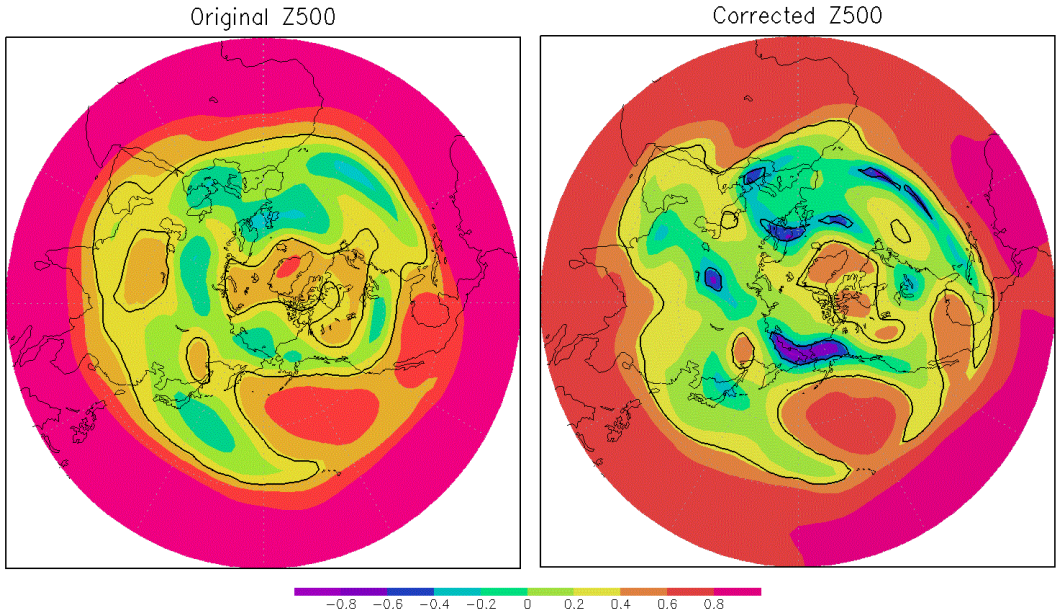

Figure 3.7: Correlation of multi-model average 500 hPa height forecasts to reanalysis for (left) before correction, (right) after correction. The black contour denotes the 95% confidence level.

To verify this hypothesis we derived the PNA and NAO indices by projecting the 500 hPa geopotential height anomalies onto rotated empirical orthogonal function loading patterns (Figure 1.1). This is done for both the reanalysis and model data to obtain a consistent set of values calculated in the same fashion. Even though the overall skill of the 500 hPa geopotential height field is lower in the "corrected" forecasts does not necessarily imply that the skill of the dominant teleconnection patterns will also be lower. Table 3.2 displays the correlation of the model derived PNA and NAO indices against those derived from the reanalysis.

Forecast Lead (months)		Lead 0	Lead 1	Lead 2	Lead 3	Lead 4	Lead 5	Lead 6	Lead 7	Lead 8	Lead 9
PNA	Original	***0.62***	***0.60***	***0.50***	***0.51***	***0.65***	***0.62***	***0.52***	***0.49***	***0.43***	0.30
	Corrected	***0.62***	***0.48***	***0.47***	***0.42***	***0.55***	***0.45***	***0.41***	***0.37***	0.25	0.05
NAO	Original	***0.48***	***0.46***	0.24	0.24	0.26	0.20	0.18	-0.01	-0.05	0.02
	Corrected	0.33	***0.35***	0.08	0.12	-0.04	-0.10	-0.10	***-0.67***	-0.27	0.12

Table 3.2: Correlation coefficient between the DJF multi-model, and reanalysis PNA and NAO indices for all lead times. Values in bold italics pass the 95% confidence level, underlined values pass the 90% significance level.

The lead time here refers to the amount of time that has passed since the initialization of the model to the target season. Therefore a lead zero forecast would mean a forecast starting on December 1st, while a lead nine forecast refers a forecast beginning on March 1st. In other words the longer the lead time, the further the target season is from the initial conditions. Table 3.2 shows that in every case the "correction" results in a lower correlation, and thus offers no improvement even in the case of large scale teleconnection patterns. Examining how the proportion of the squared covariance of each mode varies with lead time shows that while this fraction for all other modes drop after the zero-month lead, all of this variability seems to be absorbed into the first mode (Table 3.3). The dominance of the first pair of patterns (PNA and El-Nino) helps explain the skill the models possess for their PNA index forecasts. This also gives an indication as to why the variations of the NAO index are so poorly captured. With so much of the co-variance explained by the PNA and ENSO, the variability associated with the NAO may be present in the models, but simply obscured by the ensemble averaging.

Lead Time (months)	0	1	2	3	4	5	6	7	8	9	NCEP/ NCAR
SVD1	81.1	95.8	97.9	98.2	98	98.7	98.4	98.8	98.3	98.1	56.6
SVD2	10.1	1.9	1.1	1.1	1.0	0.8	0.8	0.8	1.2	1.4	20.7
SVD3	3.8	1.4	0.6	0.4	0.7	0.3	0.4	0.2	0.3	0.3	8.1
SVD4	2.1	0.4	0.2	0.2	0.1	0.1	0.2	0.0	0.1	0.1	5.5
Sum	97.1	99.5	99.8	99.9	99.8	99.9	99.8	99.8	99.9	99.9	90.9

Table 3.3: Percent of the total squared covariance explained by each pair of DJF SVD patterns and their sum for all lead times.

The models correctly reproduce the PNA variability for the majority of the year; while the NAO is predictable only about a month in advance. Given that the PNA is linearly related to

ENSO (will be shown in Section 4.1.1), it is not surprising that removing the internal variability via ensemble averaging has led to the PNA explaining the majority of the total squared temporal covariance, and significant skill for any lead time. The NAO, which explains two orders of magnitude less of the total squared temporal covariance, still displays significant skill out to the one-month lead forecast. This result is surprising since the NAO is mainly driven by internal processes (Hurrell et al. 2003). The next chapter will aim to explore the predictability sources for these two teleconnection patterns.

The statistical correction has not significantly improved the forecast skill of the 500 hPa geopotential height field, or either of the teleconnection indices. This may be due in part to the significant skill already present in the models over the majority of the Northern Hemisphere. The lack of improvement may also be due to the exclusion of SVD modes explaining as much of the total squared covariance as modes two and three. All modes generated by the SVD computation are spatially orthonormal (Bretherton et al. 1992), meaning that the exclusion of modes may reduce the forecast skill in regions dominated by these excluded modes.

To test the sensitivity of the statistical correction to the number of PC time series used, we then re-calculated the corrected forecasts in three ways: using the time series for (1) modes one, two and four, (2) the first four modes, and (3) only the first two modes. As expected, in case one the forecast skill for the NAO increased, but not above that of the un-corrected forecasts. Moreover the forecast skill for the PNA dropped and forecast skill for the 500 hPa geopotential height field was also reduced in many areas (not shown). Using the first four leading modes (case two) adds no significant benefit past the one-month lead forecasts, for which the skill in forecasting the NAO index was improved compared to both the three-SVD pattern correction and the original model output (Table 3.4). For longer lead times the skill is reduced, which is

likely related to the fact that after the one-month lead forecast none of the PC time series are significantly correlated to the NAO index. Furthermore the forecast skill for the PNA is reduced compared to the three PC time series correction. At lead times longer than a month, the fourth SVD pattern no longer resembles the NAO, and only diminishes the skill of the statistical forecasts. This can be illustrated by using only the first two PC time series for the correction (case three). In this case the forecast skill for the PNA has extended out to the eight-month lead forecast as in the original model output (Table 3.4). The skill for the PNA marginally increases compared to the three PC correction because the number of modes whose variability is unrelated to the PNA has been removed; similarly all skill for the NAO has vanished since any mode of variability related to it has been excluded. We can therefore conclude that the variability of the NAO relating to the Tropical Pacific SST is therefore either located in modes three and/or four (or even lower mode of variability) or is non-linearly related to the SST in this region. In any case the correction process yields no statistically significant benefit.

Forecast Lead Time (months)		Lead 0	Lead 1	Lead 2	Lead 3	Lead 4	Lead 5	Lead 6	Lead 7	Lead 8	Lead 9
No Correction	PNA	**0.62**	**0.60**	**0.50**	**0.51**	**0.65**	**0.62**	**0.52**	**0.49**	**0.43**	0.30
	NAO	**0.48**	**0.46**	0.24	0.24	0.26	0.20	0.18	-0.01	-0.05	0.02
Correction with 2 PCs	PNA	**0.64**	**0.52**	**0.48**	**0.43**	**0.55**	**0.51**	**0.43**	**0.37**	**0.34**	0.14
	NAO	0.27	0.03	0.06	0.19	0.00	-0.09	-0.12	**-0.51**	-0.18	**-0.38**
Correction with 3 PCs	PNA	**0.62**	**0.48**	**0.47**	**0.42**	**0.55**	**0.45**	**0.41**	**0.37**	0.25	0.05
	NAO	0.33	**0.35**	0.08	0.12	-0.04	-0.10	-0.10	**-0.67**	-0.27	0.12
Correction with 4 PCs	PNA	**0.40**	**0.37**	**0.38**	0.22	**0.44**	**0.36**	0.24	**0.37**	0.15	0.03
	NAO	**0.38**	**0.47**	0.07	0.05	-0.08	-0.04	-0.01	**-0.35**	0.09	-0.03

Table 3.4: Forecast skill of multi-model PNA and NAO indices for all forecast lead-times and correction procedures.

4 Predictability Sources of the Teleconnection Patterns

4.1 Link to ENSO

4.1.1 PNA

Table 3.2 poses some interesting questions: Why is the PNA predictable nine months in advance? What are the sources for this skill and that of the NAO? These questions will be addressed in the following sections. The PNA has been found to be predictable during extreme ENSO events (Derome et al. 2005); however that study used persisted SST anomalies over the forecast period. This method is able to produce significant skill in the 500 hPa geopotential height field over the Northern Hemisphere when the forecast period is a season or less (e.g. Derome et al. 2001). The present study makes use of two fully coupled models, where the atmospheric and oceanic components can communicate and evolve in tandem. Latif et al. (1994) demonstrated that the tropical Pacific SST anomalies can be skillfully predicted as much as a year in advance, which would indicate that if this is the case for the CanSIPS models, the PNA index should be predictable, at least partially, for similar lead times.

The CanSIPS models can indeed skillfully predict the SST in the tropical Pacific given a nine-month lead until the target season (i.e. forecast initialized in March) (Figure 4.1). This explains the significant skill observed for the predicted PNA index. The temperature pattern associated with the PNA circulation also appears with significant skill. The warm anomaly over Alaska, due to the circulations of the Aleutian low and the high pressure centre over western North America (Figure 1.1), is present in the models (Figure 4.2b). These circulation patterns work in unison to advect warm air from low latitudes up North. The cold anomalies over the

North Pacific and South-eastern United States are similarly driven by the high over western North America and the low centred over Florida (Figure 1.1), which together act to advect cold air from North-eastern Canada to the southern states; again present in the models (Figure 4.2). These patterns are slightly displaced to the West of position in which we would expect (compare with Figure 4.2a). This phenomenon is due to the westward extent of the ENSO related SST anomalies. Since the boundary forcing extends too far to the west we see a similar shift in all associated temperature and pressure patterns (Merryfield et al. 2013).

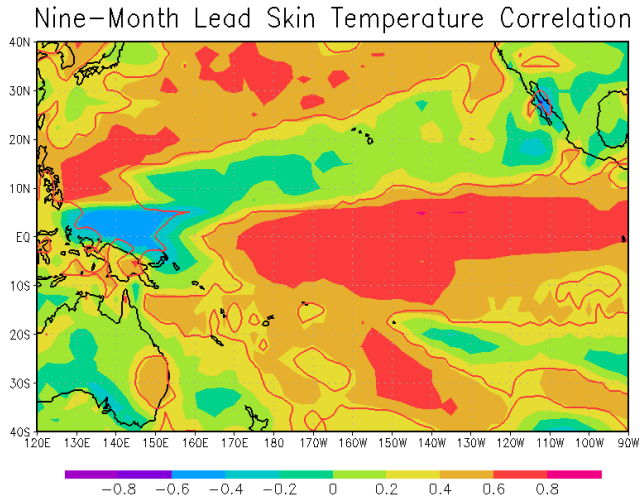

Figure 4.1: Correlation of 9-month lead DJF Multi-Model SST with reanalysis SST. Areas inside the red contour pass the 95% significance level.

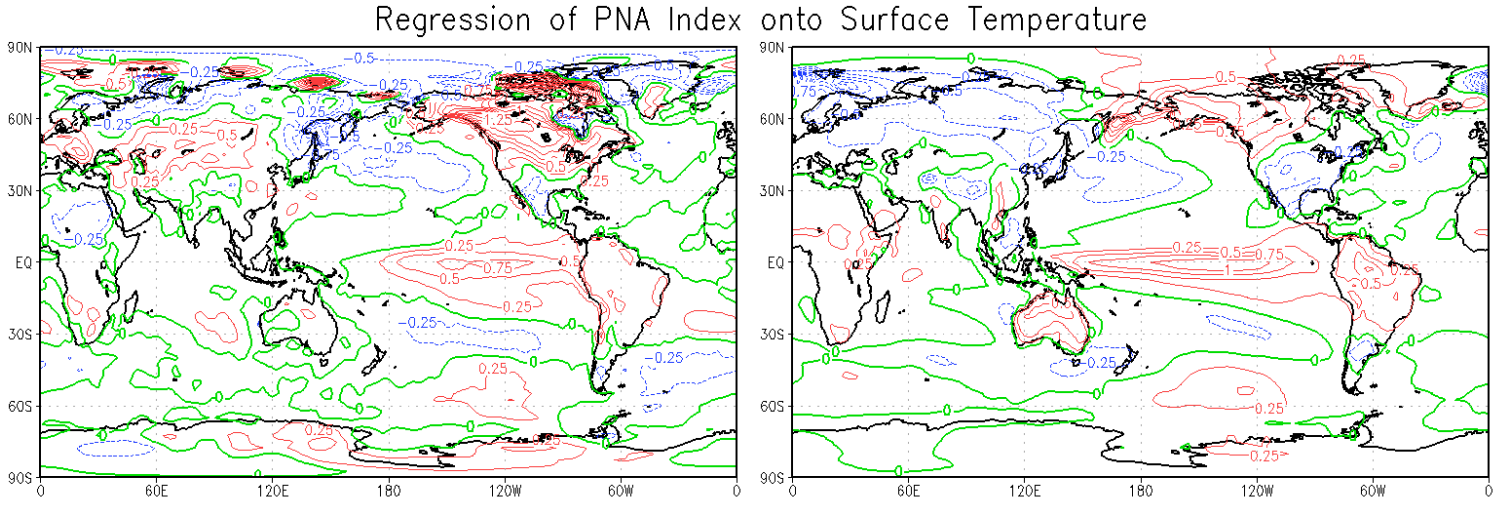

Figure 4.2: Regression of PNA index onto surface temperature for (left) reanalysis field, and (right) nine-month lead multi-model field. The magnitude corresponds to the temperature increase associated with an increase of 1 standard deviation of the PNA index.

There are however some notable differences between Figures 4.2a and b; the cold anomaly over northern Eurasia, and the warm anomaly over Africa. These kinds of anomalies are generally associated with the negative phase of the NAO. These issues will be addressed in more detail in the following sections.

To further cement the relationship between ENSO and the PNA, the Nino-3.4 index was calculated for each forecast lead time as well as for the reanalysis data sets. This index is simply the area averaged SST anomaly in the region of 5^{o}S -5^{o}N, 190^{o}E-240^{o}E normalized by the standard deviation of the time series. This simple index provides a proxy for the phase and amplitude of El-Nino events. Given that the area where this index is calculated exhibits high correlation with the reanalysis data and very little bias, one would expect the index to have an even higher correlation than the field itself. This is in fact the case; the correlation between the reanalysis Nino-3.4 index and that of the model exceeds the 99% significance level for all lead times (Figure 4.3). To a good first approximation, the CanSIPS models are able to skillfully predict the phase and amplitude of El-Nino events up to nine months in advance. The link between the PNA and ENSO is well documented (e.g. Horel and Wallace 1981; Mo et al. 1998) and is present within the CanSIPS models for all lead times(Table 4.1). This relationship is quite strong in the reanalysis data, and even stronger in the models. The zero-month lead forecast is influenced by the initial conditions of the model, and has a correlation close to that of the reanalysis data. All subsequent lead times correspond to when the target season is outside the range of influence of the initial conditions, and more heavily influenced by the boundary forcing. It is not unexpected to see a rise in the correlation coefficient after this point; especially since the internal variability has been filtered out. This increase in correlation also reflects the increase of explained variance by the PNA/ENSO SVD mode (Table 4.1).

Lead Time (months)	0	1	2	3	4	5	6	7	8	9	Reanalysis
Correlation	0.56	0.86	0.88	0.95 (0.92)	0.88 (0.88)	0.90 (0.90)	0.89 (0.89)	0.90 (0.90)	0.92 (0.93)	0.86 (0.86)	0.53 (0.58)

Table 4.1: Correlation between Nino-3.4 Index and PNA index. ALL values pass the 99.9% significance level. Values in parentheses indicate correlation using the preceding September-November Nino-3.4 index.

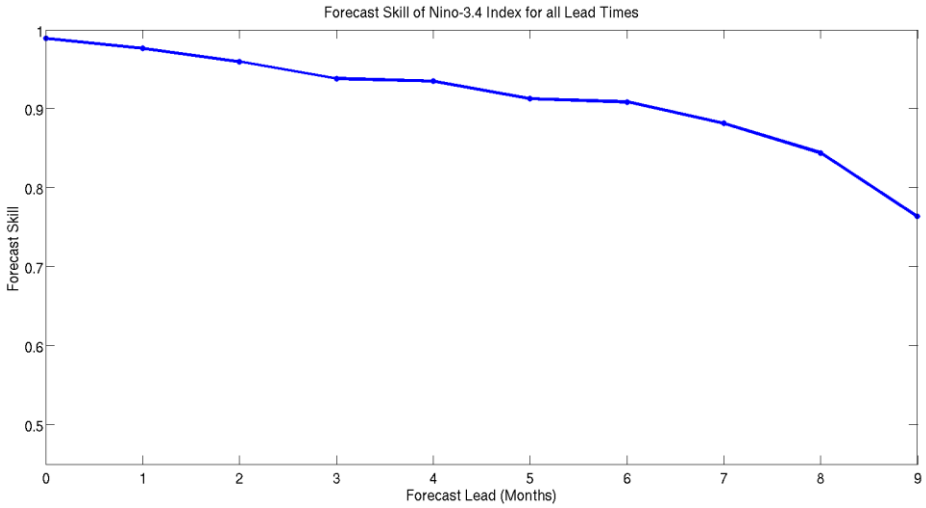

Figure 4.3: Forecast skill of the Nino-3.4 index for all forecast lead times. The bottom of the plot (0.45) corresponds to the 99% significance level.

Finally, Mo et al. (1998) found that the PNA is most strongly related to the El-Nino signal from the preceding season (i.e. September-November). The regression of the winter PNA index onto the fall surface temperature field (not shown) yields the temperature pattern which *forces* the PNA, since these patterns occur a season in advance. Only two anomalies remain in the reanalysis data: a stronger ENSO type anomaly and a cold anomaly in the south Pacific around 30ºS (both visible in Figure 4.2a). These persistent anomalies account for the higher correlation between the fall SST and winter PNA index (Table 4.1; reanalysis column). The

regression of the multi-model PNA index onto the surface temperature (not shown) displays temperature patterns over land commonly associated with the *forcing* of the PNA (i.e. warm west coast, cold southeast North America). These temperature patterns should not be present given that they are supposed to be the result of a positive PNA, not the boundary forcing responsible for producing a positive PNA. Given that these patterns have not changed it is possible that the ocean does not evolve realistically within the models. Moreover it is not surprising that the correlation within the models does not improve.

The first pair of SVD patterns (Figures 3.5 and 3.6) show that the PNA is associated with a strong anomaly in the Tropical Pacific Ocean. Previous studies have found similar results, whereby the PNA is most highly correlated with the "extreme" phase of ENSO, while the "non-extreme" events are significantly correlated with the NAO (Derome et al. 2005) (Table 4.2). We make use of the Nino-3.4 index previously calculated and take the years in which the index is within one standard deviation. Of the 32 years, 20 fall into this category with the remaining 12 are classified as "extreme" ENSO events. Even though there are only 12 "extreme" years, the correlation with the PNA index still passes the 99% significance level (Table 4.2), and is higher than that of the one-month lead forecast in Table 4.1. This result shows that the majority of the predictive skill associated with the PNA comes from extreme positive ENSO years. The models depict a slightly different relationship (Figure 4.4). Here the PNA is linearly related to any phase of ENSO, meaning that the stronger the ENSO event (either positive or negative), the stronger the PNA pattern will be. This would seem to imply that the internal dynamics play a larger role in negative and non-extreme ENSO events (Table 4.2), since the reanalysis PNA index only displays a strong linear relationship with positive events (Figure 4.4; left).

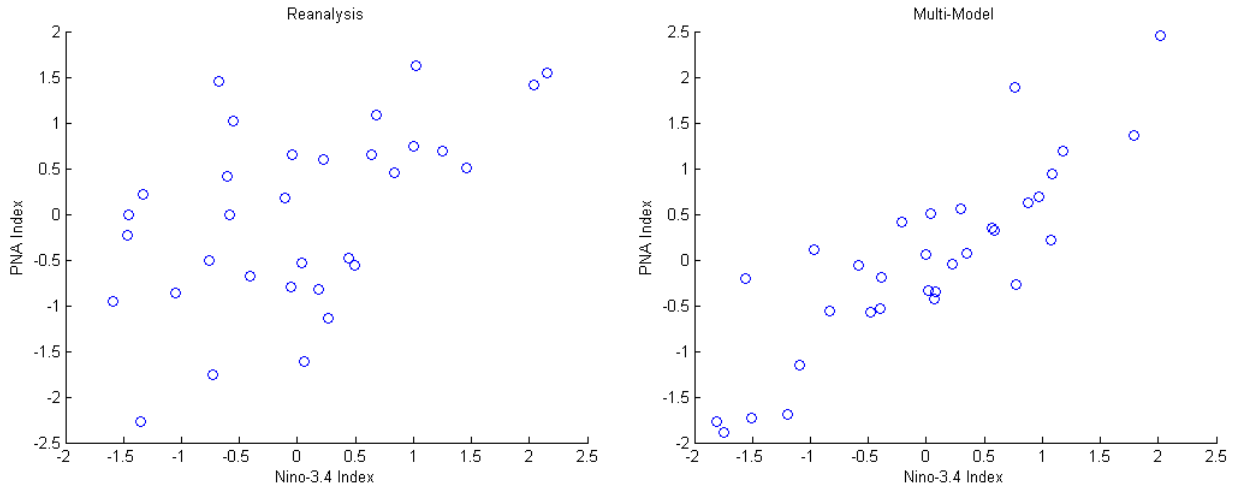

Figure 4.4: PNA index plotted against the Nino-3.4 index for (left) reanalysis, and (right) one-month lead multi-model quantities.

4.1.1 NAO

In this section we explore the link between ENSO and the NAO. In chapter 3, the SVD analysis between the tropical Pacific SST and the northern hemisphere geopotential heights yielded the NAO pattern (Figures 3.5 and 3.6 right panels). This result implies that there exists some link between the NAO and the tropical Pacific SST. From these figures we can see that the link appears to be when the magnitude of the SST anomaly is rather small. The skill for the NAO, based on the partitioning the data based on the sign and phase of ENSO events, shows that the correlation of the NAO index with the "non-extreme" ENSO years is much higher than that of the PNA; however it does not pass the 90% significance threshold. When comparing these results to those of the models two things are immediately evident: 1) the correlation coefficients are all higher than those of the reanalysis quantities, and 2) the sign of the correlation coefficient of the NAO with "non-extreme" ENSO years is inverted. The higher correlation coefficients are most likely due to the removal of the internal variability. The inverted sign of the correlation

coefficient between the NAO and "non-extreme" ENSO years indicate that the models may not be capturing some aspect of the NAO's variability. To explain these discrepancies, we examine the scatter plots of the NAO index against the Nino-3.4 index for both the reanalysis and the multi-model average to get an idea of how the models represent the relationship versus the actual relationship (Figure 4.5).

		Extreme	Non-extreme	ENSO+	ENSO-
Reanalysis	PNA	0.80 (0.00)	0.08 (0.74)	0.76 (0.00)	0.32 (0.23)
	NAO	-0.21 (0.52)	0.33 (0.16)	-0.00 (1.00)	-0.20 (0.45)
1-month lead Multi-Model	PNA	0.93 (0.00)	0.60 (0.01)	0.71 (0.00)	0.69 (0.00)
	NAO	-0.72 (0.01)	-0.62 (0.00)	-0.56 (0.02)	-0.44 (0.09)

Table 4.2: PNA and NAO indices correlated with Nino-3.4 index for various ENSO phases. An extreme ENSO year is defined as a year whose Nino-3.4 index surpasses 1 standard deviation, non-extreme encompasses the rest. ENSO+(-) refers to a portioning based on the sign of the index. Values in parentheses are p-values.

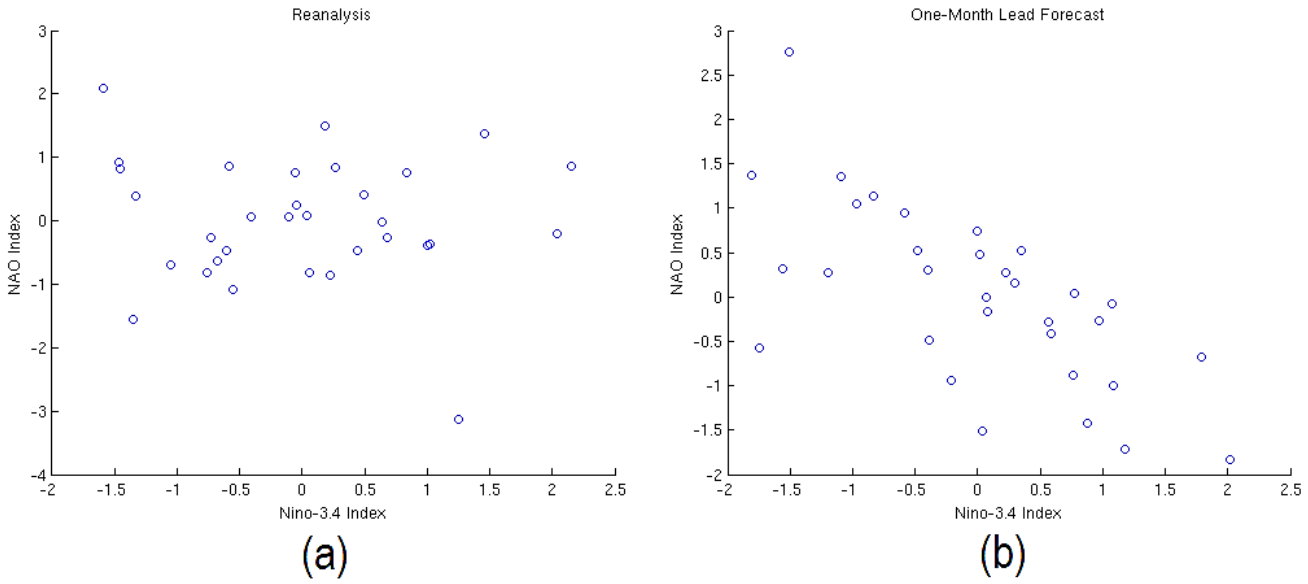

Figure 4.5: NAO index versus Nino-3.4 index for (a) reanalysis, and (b) 1-month lead multi-model average.

The above scatter plots are for the un-partitioned indices (as in Figure 4.4), and as such display similar information as Table 4.2. These plots do however aid in understanding the discrepancies between the reanalysis and multi-model correlation coefficients. From Table 4.2 we find that the NAO is linked to the tropical Pacific through non-extreme ENSO events (Derome et al. 2005), and to a lesser extent negative ENSO events (Pozo-Vázquez et al. 2005). Figure 4.5 (left panel) depicts a similar relationship; while it is true that the NAO is positively correlated to non-extreme ENSO events, it is also negatively correlated with negative ENSO events. If we examine the entire data set instead of portions of it another relationship appears. Both strong positive and negative ENSO events, in general, force a positive NAO pattern (Wu and Hsieh 2004). Even though this result does not pass any important significance level, it still hints at the nonlinearity inherent within the NAO. This nonlinearity does not appear in the models (Figure 4.5; right panel). A strong negative linear trend is instead apparent. This indicates that the models only represent the linear relationship between the NAO and ENSO. If we assume a quadratic relationship (as was found in Wu and Hsieh 2004), and fit a curve to the reanalysis data (not shown), we see a concave curve, consistent with strong negative and positive ENSO events forcing a positive NAO pattern (Lin and Derome 2004). Similarly if we fit a straight line to this same data, the slope is negative. This all appears to confirm that the models do a good job representing the linear relationships, such as the relationship between ENSO and the PNA, but are deficient in representing nonlinear relationships.

4.2 The North Atlantic Ocean's Relationship to the NAO

Here we consider the NAO's relationship to the Atlantic Ocean. Given that the pressure anomalies which comprise the NAO are situated in the Atlantic Ocean we may expect SST anomalies in the area to either force, or modulate the strength of the NAO. To verify if such a relationship exists, we take the regression of the SST onto the NAO index. This provides an image of the temperature change associated with a change of one standard deviation of the NAO index. The simultaneous SST regression patterns for the Atlantic Ocean display a weak tri-pole SST pattern associated with the NAO (Lin and Derome 2003) (Figure 4.6).

This pattern is composed of positive values extending from the eastern United States to the United Kingdom, with negative values on either side. The second mode of the reanalysis and the fourth mode of the models yield almost identical figures (Figure 4.7), cementing the interpretation of the fourth SVD mode being associated with the NAO. The models represent this tri-pole pattern fairly well, especially in terms of location and amplitude. There are some differences however; the amplitude of these temperature anomalies remains too weak in several regions. These shifts may be indicative of a too quickly evolving ocean, whereby the tri-pole pattern depicted below evolves from a more horseshoe-type pattern in the late fall, categorized by a south-ward shift of all anomalies (Czaja and Frankignoul 2002; Lin and Derome 2003). This shift can be seen in both the multi-model regression and SVD figures.

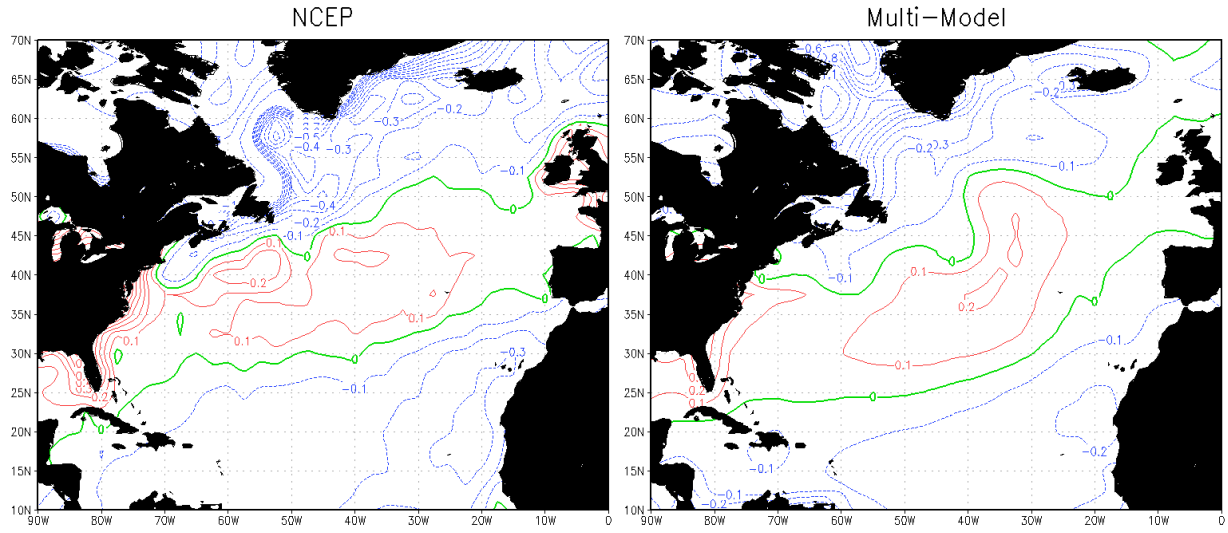

Figure 4.6: Regression of SST anomalies onto the NAO index. The magnitude corresponds to the temperature change associated with a change of one standard deviation of the NAO index. Note that the contour levels above 1 and below -1 are incremented by 1 instead of 0.1.

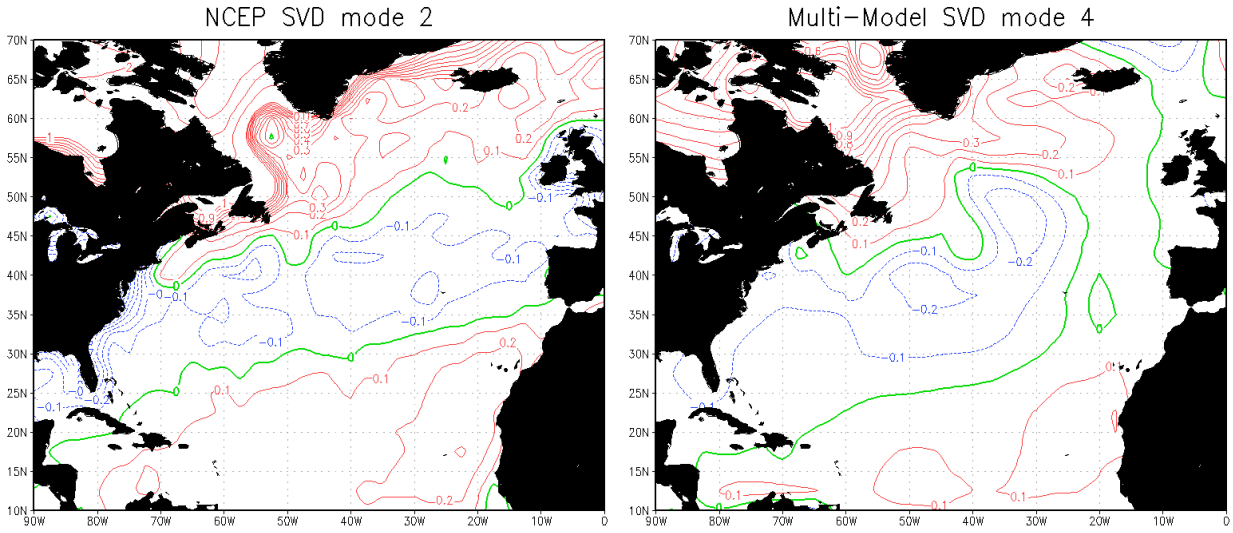

Figure 4.7: Regression of SST anomalies onto the (left) reanalysis and (right) one-month lead multi-model PCs. The magnitude corresponds to the temperature change associated with a change of one standard deviation of the PCs. Note that these pattern are for the negative phase of the NAO. Values in excess of +/- 1 are incremented by 1.

The question then becomes whether this pattern's time series is correlated with the NAO, and whether the structure is reproduced by the models. This is examined by first conducting an SVD analysis between the Northern Hemisphere 500 hPa geopotential heights and the skin

temperature between 10-70°N and 270-360°E to verify that this pattern is indeed related to the NAO. Secondly we examine the pattern from the seasons before and after to verify that the evolution of the pattern is well defined. Both the reanalysis and multi-model average reproduce the NAO and the SST tri-pole in their first 500 hPa height and SST patterns, respectively (Figure 4.8). They display the same properties as the SVD using the Pacific SST and regression patterns (Figures 4.6 and 4.7). This tri-pole SST pattern is therefore the leading mode of variability associated with the NAO in the Atlantic region. These "Atlantic SVD" patterns correlate more significantly with the NAO than the Pacific ones in all cases, especially in the multi-model temperature field (Table 4.3). This analysis shows that a relationship exists, given that both the reanalysis and models associate this SST pattern with the NAO regardless of the SST domain used for the SVD analysis.

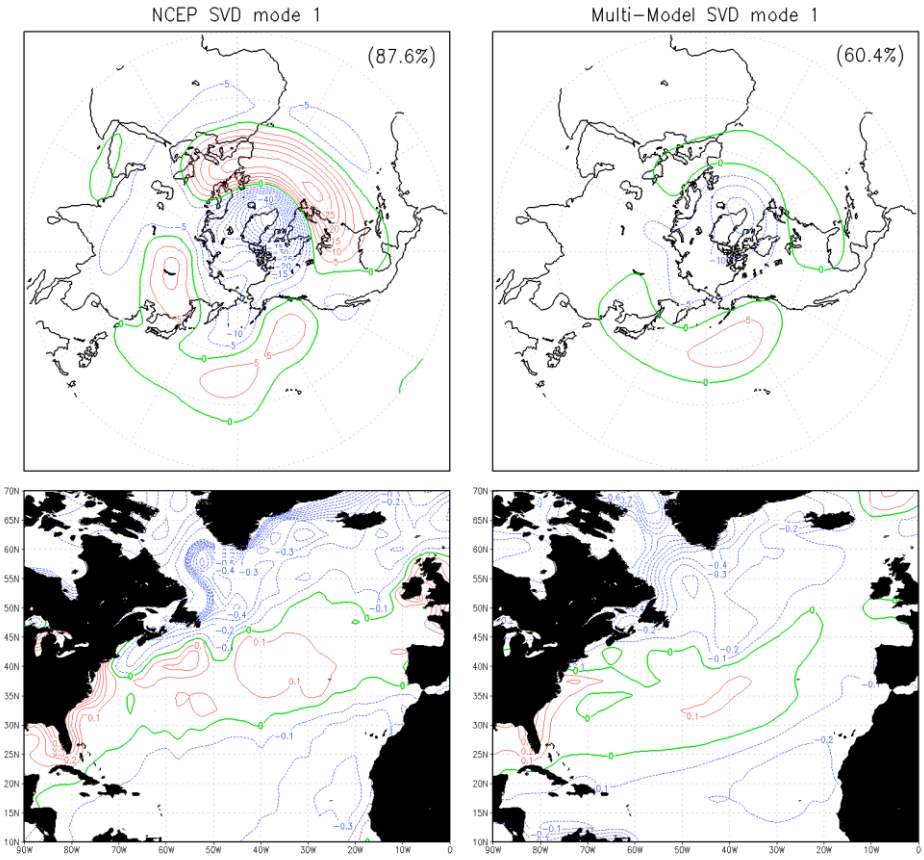

Figure 4.8: Projection of (top) 500 hPa height anomalies, and (bottom) SST anomalies onto the first Atlantic SVD mode PCs. Note that values exceeding +/-1 are incremented by 1.

Correlation with DJF NAO		Pacific SVD mode 4 PC	Atlantic SVD mode 1 PC
Reanalysis	Z500	**-0.95**	**0.99**
	SST	**-0.80**	**0.82**
Multi-Model	Z500	**-0.67**	**0.92**
	SST	-0.29	**0.57**

Table 4.3: Correlation of PCs from both SVD analyses with the NAO index. Bold values pass the 95% significance level.

These "Atlantic" PC time series are more significantly correlated with the reanalysis NAO index than the multi-model NAO index is (> 0.50). This means that these patterns better represent the time variation of the NAO index than the 500 hPa geopotential height anomalies. As such we examine how the Atlantic Ocean varies with the NAO, and how the ocean forces, and reacts to, the NAO in a season prior and several seasons after DJF, using the first Atlantic 500 hPa height PC as a proxy for the NAO index. The SST is regressed onto this PC time series for two seasons preceding winter, and the spring to attempt to capture the feedback described by (Czaja and Frankignoul 2002). Their feedback loop between the tri-pole pattern, the NAO, and the "horseshoe" pattern entails the NAO forcing a modulation of the amplitude of the tri-pole pattern, which then directly affects the intensity of the "horseshoe" pattern into which it evolves due to advection. The SST then feeds back into the NAO, where a stronger "horseshoe" pattern forces a stronger NAO; and thus the positive feedback loop is closed. The "horseshoe" pattern depicted (Figure 4.9 top left) clearly undergoes an evolution which begins prior to November, and continues through to the spring. This evolution is characterized by a southward expansion, and northeast- and southwest-ward extension of the positive temperature anomaly from September to December. Over the late winter and early spring all temperature anomalies associated with the winter NAO intensify (Czaja and Frankignoul 2002). There is no analogous pattern to the "horseshoe" pattern within the multi-model average.

To verify that the models capture this feedback we conduct this same SVD analysis using the September initialized forecast, to regress the 500 hPa height PC related to the NAO onto the SON (September-November) SST (to generate a figure analogous to Figure 4.9's top left panel). The NAO height and temperature patterns (both tri-pole and horseshoe) are not reproduced (not shown). In the reanalysis data the tri-pole pattern obtains its maximum amplitude in the spring, showing that the NAO forces this SST pattern. The models depict a weakening starting in NDJ and ending in the spring (Figure 4.9), meaning that this relationship is not present.

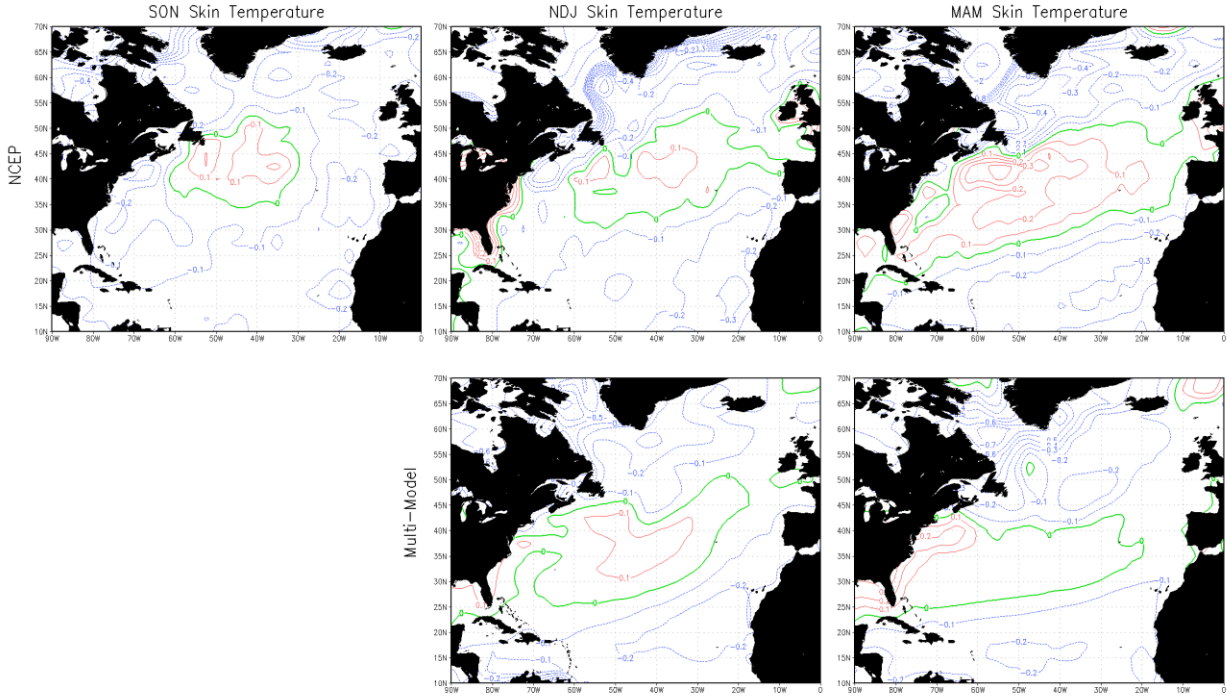

Figure 4.9: Regression of the (top) NCEP, and (bottom) multi-model first 500 hPa geopotential height PC onto the corresponding skin temperature field for seasons preceding (left and centre), and after (right) the DJF season. The amplitude corresponds to the temperature change associated with an increase of one standard deviation of the PC. Values in excess of +/-1 are incremented by 1.

4.3Eurasian Temperature and Snow Depth

4.3.1 NAO

While the oceans provide a very predictable and slowly-varying boundary forcing, it is not the only one. Studies over the past decade have begun to link hemispheric geopotential height anomalies to snow cover, snow depth, and temperature over the Eurasia landmass. Asia, and Russia in particular, is the largest expanse of land in the Northern Hemisphere, and the temperature variations of such a large landmass have the potential to affect the downstream flow patterns (Figure 4.10). Along with showing the North Atlantic temperature tri-pole pattern discussed above, Figure 4.10 also reveals another feature common to both the models and the reanalysis data. Both images show a positive correlation with temperatures extending from northern Europe through Russia, with negative correlations prevailing south of 45^{o}N. The NAO tends to be associated with this kind of temperature pattern (van Loon and Rogers 1978; Rogers and van Loon 1979), although since boundary conditions, such as land temperature and snow depth vary slowly, there may be some signatures in the area which precede the NAO.

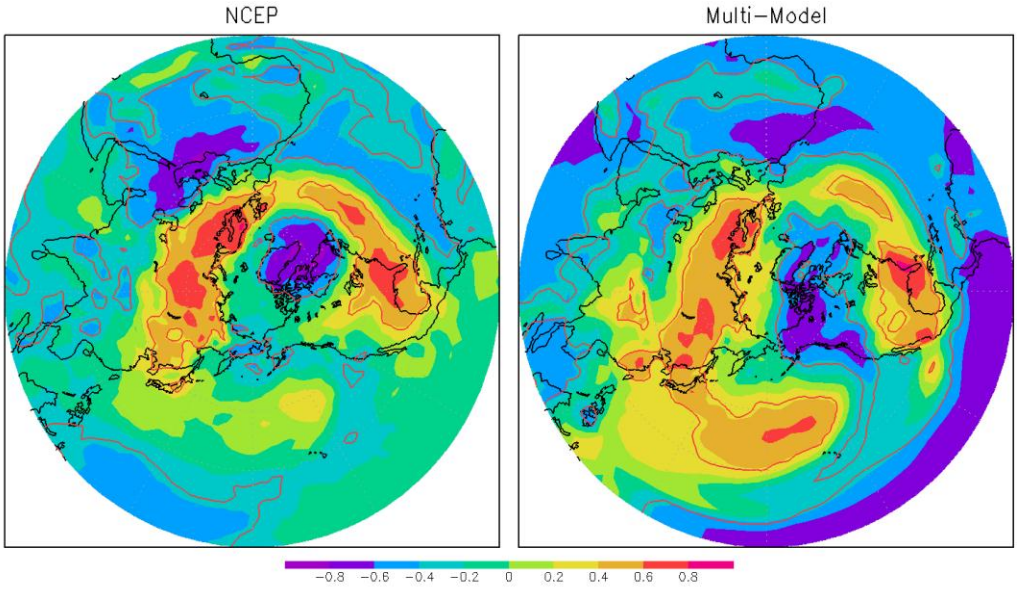

Figure 4.10: Simultaneous correlation of near-surface air temperature with the NAO index. Red contours denote regions passing the 95% significance level.

In this section we examine whether the models can depict the same spatial pattern of correlation as the reanalysis between the near-surface air temperature and snow depth, and the NAO index. Other than the ENSO signature which is ever present, there is good agreement across northern Europe, Russia, North Africa and the Middle East (Figure 4.10). These panels reveal a large area of positive correlation extending from Europe across northern Russia. This large scale temperature pattern is associated with one of the semi-permanent pressure systems of the Northern Hemisphere, the Siberian High (Cohen et al. 2001). Siberia is the largest contiguous landmass of the Northern Hemisphere, and it has relatively little elevated terrain. The variability of the overlying temperature of such an area can act to modulate the amplitude and phase of the NAO. To attempt to determine possible sources of predictability for the NAO examining the winter conditions yields vague results, as it is impossible to separate the forcings from the effects using techniques described in Chapter 2.

The DJF temperature in this area has been shown to be correlated to the autumn area averaged snow-cover (Foster et al. 1983). Furthermore during the fall and winter, snow-cover exhibits large spatial and temporal variability (Foster et al. 1983; Robinson et al. 1993), providing a potential source of climate variability and more importantly, predictability. Unfortunately the CanSIPS models do not store the snow-cover, only the snow depth. In general the fall snow depth does show a negative correlation with fall temperature over Europe and southern Russia (not shown); yet the lead-lag relationship only exists for the areal average and a few minute locations over western and northeastern China. The comparison of the model snow depth with the reanalysis snow depth has proved impossible. Each are output on different grid formats and when attempting to convert between the two the data is distorted in such a way as to render it useless. As a result, a simple index was created using the same approach as to calculate

the Nino-3.4 index. The areal average over 20-70N, 60-120E for the near-surface air temperature and snow-depth is normalized by the standard deviation to generate both indices. For this area, the fall snow depth index (SDI) is strongly correlated with its model counterpart, and furthermore, the fall SDI is correlated with the November temperature index (calculated in the same way), thus preserving the lead-lag relationship (Table 4.4). Note again that the fall SDI is calculated using the September initialised forecast, while the November temperature index displayed hereunder is from the November initialised forecast. Using the September forecast run to calculate the Temperature index yields similar results (not shown). The purpose of cross comparing forecast runs is twofold; first, to verify the consistency of the temperature forecast, and second is that only up to the one-month lead (November initialised) forecast of the NAO index is significant. Continuing to use the September forecasts would be pointless since the NAO itself is not correlated with the reanalysis NAO index. Therefore the goal is to determine whether the Temperature index calculated from the November forecast run can be used as a proxy for the fall (September initialised) SDI. To further support the choice of temperature over snow depth, referring back to Table 2.1, the reanalysis snow depth data is entirely model derived, whereas the near-surface air temperature has observational input, making it a more reliable data source. The correlation of the model SDI with the reanalysis temperature index (and vice versa) show that they do indeed vary together quite closely. The results displayed in Table 4.4 seem to support the use of the late fall temperature as a proxy for the total fall snow depth. Nevertheless, maps using fall snow depth will still be shown, and will be supported by a corresponding late fall temperature plot where appropriate. The plots of snow depth should be interpreted with caution given their unreliable nature.

Corr (passed significance level %)		Multi-Model Indices		Reanalysis Indices	
		SON SDI	Nov Temp	SON SDI	Nov Temp
Multi-Model Indices	SON SDI	-	**-0.53**	**0.61**	**-0.42**
	Nov Temp	-	-	**-0.55**	**0.58**
Reanalysis Indices	SON SDI	-	-	-	*-0.30*
	Nov Temp	-	-	-	-

Table 4.4: Correlation of SDI with the Temperature index. Values in italic, and bold pass the 90%, and 95% significance level respectively.

There has been growing interest over the past decade in the relationship between the snow cover (and temperature) over Eurasia and the NAO (e.g. Bamzai 2003; Gong et al. 2003; Saito et al. 2001; Seager et al. 2010); however there is still debate as to whether the NAO forces snow-cover anomalies, or if these anomalies excite the NAO in the subsequent season. Since the purpose of this study is to determine possible predictability sources for the NAO, we will focus on snow (and temperature) anomalies preceding the NAO. These, and the other previously mentioned studies, either solely use observational data, or atmospheric models in conjunction with observations, whereas the CanSIPS models are fully coupled. It is therefore of interest to examine whether these models can capture relationships seen in the reanalysis data.

Continuing to examine the simple indices for temperature and snow depth, we can verify if the models can pick up the large scale, area averaged relationship between these indices and the winter NAO (Table 4.5). The correlations of these indices within the reanalysis data pass the 90% significance level, indicating that some sort of signal over Eurasia exists which precedes the NAO. When comparing these values to those derived from the model indices, we see that the model indices display no significant correlation. While the models may not capture the large scale pattern, they may capture some smaller scale features which are averaged away by the calculation of the index. This hypothesis is easily verified by plotting maps similar to those

presented in Figure 4.10, but using the late fall temperature from the November initialized forecast (zero-month lead) and complete fall snow depth field from the September initialized forecast (three-month lead) (Figure 4.11). We can see large-scale discrepancies between the relationship of the reanalysis snow depth and NAO, and the relationship captured by the models. Most noticeable are the large areas of negative correlation in the models, over areas just north of where the reanalysis snowline is located (where the colour shading ends), particularly in the central United States, and Iran, Turkmenistan, and Afghanistan. These are areas of no significant correlation in the reanalysis. The large area of negative correlation over China and Mongolia present in the reanalysis has been reduced to a few small areas of local significance. Similarly the large area of positive correlation south of the Scandinavian countries has also been reduced in size.

Correlation with DJF NAO index	Multi-Model	Reanalysis
November Temperature Index	0.14	*0.30*
November SDI	0.08	0.16
SON SDI	-0.06	*0.31*

Table 4.5: Correlation of Eurasian Indices with DJF NAO index. Values in italics pass the 90% significance level.

The relationship between both the snow-depth and the temperature and the NAO depicted by the reanalysis fields, show a significant relationship over Northeast China (Figure 4.11; top panels). These results are consistent with those of Jia et al. (2014) which showed that this region is significantly correlated to the second SVD mode (associated with the NAO; see Chapter 3) between the tropical Pacific and Northern Hemisphere geopotential heights (same region as used here). This temperature pattern is associated with the evolution of the Siberian High over the late

fall and winter seasons (Cohen et al. 2001). This region is also strongly affected by the East Asian Winter Monsoon, whose relationship with the NAO may occur through a mutual relationship with the Siberian High (Gong et al. 2001). Although in this case the NAO would be forcing the temperature anomaly in China instead of the other way around. This broad area of high correlation shows remarkable consistency between the reanalysis snow depth and temperature plots. The models show some areas of more localized correlation; along the eastern coast of China in the snow depth plot, and a few patches along 40°N extending from eastern China towards the Himalayas. One large feature missing from the model plots is the area of correlation which is supposed to be located over Western Europe. This cold anomaly must therefore be associated with a process related to the NAO which the models cannot reproduce given that it is present is both variable fields.

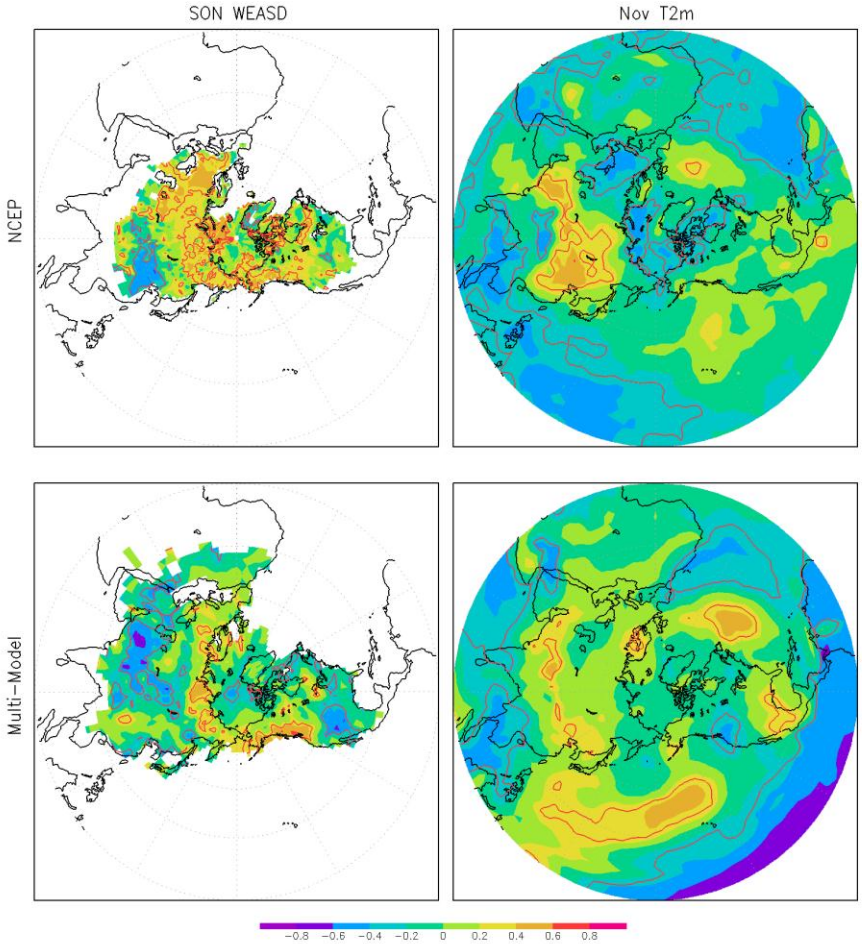

Figure 4.11: Correlation of Fall (SON) water equivalent of snow depth (WEASD) and November 2m Temperature with the DJF NAO index. Red contours outline areas which pass the 90% confidence level. Note that the bottom panels are from two separate model realisations.

Cohen et al. (2002) revealed that there are two distinct pathways that can be followed during the formation of the NAO. The first involves a high pressure system originating over eastern Siberia, propagating north and west across the Arctic to where it eventually settles over the North Atlantic and Arctic Oceans. Siberia is a location of enhanced upward wave activity flux during the fall preceding the NAO (Gong and Entekhabi, 2003). When the pressure system that eventually forms the high of the negative NAO originates in this area, this energy anomaly causes zonal wind anomalies, which are propagated into the stratosphere where they are reflected back down towards the troposphere and generate a more zonally symmetric NAO. This pathway generates a temperature anomaly covering northern China, Mongolia, and southeastern Russia in November (Cohen et al. 2001, their Figure 2b). The second, more common, pathway involves the high pressure originating in the North Atlantic. Here the NAO anomaly forms more slowly during the fall, and only develops in the early winter; it is therefore decoupled from the stratosphere (Cohen et al. 2002). The high expands into Europe and eventually generates a more regionally manifested NAO. The main difference (depicted by comparing Cohen et al. 2002 Figures 1 and 3) is the location of the high pressure system. The more zonally symmetric manifestation of the NAO has its high centred over the Arctic Ocean; whereas the more regional manifestation has the high skewed more towards the North Atlantic Ocean. The temperature patterns which are associated with each of these pathways are distinct. The regional manifestation of the NAO has a pressure anomaly located over Europe which retracts north to rest over Scandinavia for the later portion of the month, bringing warm temperatures with it. On the other hand the zonally symmetric NAO has a temperature anomaly located over Eastern Siberia and Northern China where the high originated (Cohen et al. 2001; their Figure 2). The temperature anomaly located over Russia is present in the models while there is no relationship

with Europe. This may signify that the models only capture one of the two pathways. If this is indeed the case, this provides a possible reason for the rather poor skill in predicting the NAO. Another possibility (which will be touched upon in Chapter 5), is a misrepresentation of the Atlantic storm track's association with the NAO.

4.3.2 PNA

There have also been studies linking the fall snow cover over Tibet to the PNA (Lin and Wu 2011; Wu et al. 2011). The snow cover over the Tibetan Plateau was shown to be positively correlated to the Nino-3.4 index, and to the first PC of North American temperature, associated with the PNA. This pattern of correlation has proved completely undetectable in the reanalysis temperature field (Figure 4.12; top), and snow depth field (not shown) even after lowering the significance threshold to the 90% level. The model fields do capture regions of positive correlation for snow depth (assuming snow depth and snow cover are positively correlated), and match it with a region of negative correlation in the temperature field (Figure 4.12; bottom). Many of these regions are similar to those in Figure 4.11 (bottom left panel). The regions which are not represented in the top panels of Figure 4.11 are probably associated with the PNA within the models due to the ENSO related forcing seen in all multi-model correlation plots thus far, but present in both sets of figures due to the high correlation between the modelled PNA and NAO indices (-0.70). However, within the models, the area of correlation in the Tibetan Plateau region does appear larger in the PNA figures than the NAO figures. While the models do seem to

reproduce the results of the aforementioned studies, the relationship is absent from the reanalysis data, possibly due to the different variables used herein.

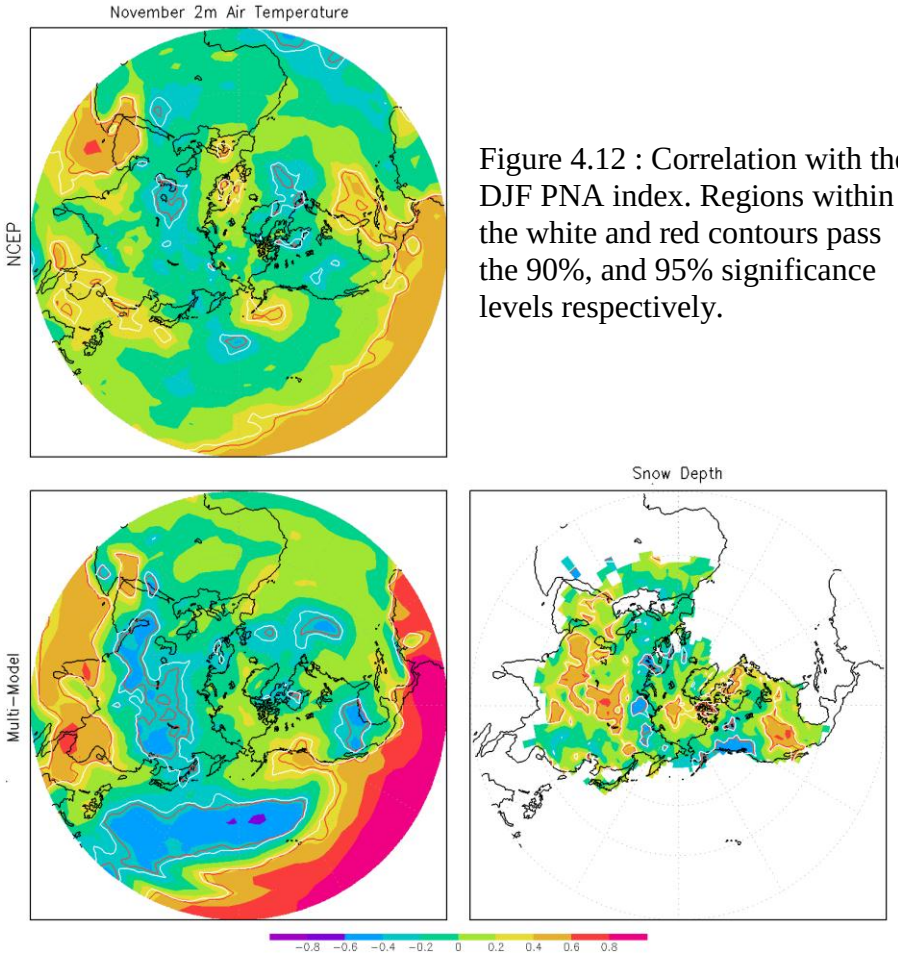

Figure 4.12 : Correlation with the DJF PNA index. Regions within the white and red contours pass the 90%, and 95% significance levels respectively.

5 High- and Low-Frequency Eddies

5.1 Representation of Low-Frequency Eddies

The 500 hPa geopotential height field is dominated by the low-frequency eddies and has two major centres of variability: one located atop the Aleutian Islands, and the second over Iceland (Blackmon 1976). These two centres correspond to pressure centres associated with the PNA and NAO respectively. Referring back to Figure 3.1, note that the locations of the troughs and ridges, while quite similar between the reanalysis and multi-model average, do display subtle differences. First, the slight ridge over the Tibetan Plateau is more pronounced in the reanalysis, the isopleths are more compact in the trough over the Pacific Ocean, and the trough over the Atlantic Ocean is displaced to the east in the models. Of note is the ridge over the Rocky Mountains which is seen to be in the correct location and of the correct amplitude. All of these characteristics are also apparent in Figure 3.2 as previously noted. Some of the differences manifest themselves in the low-frequency eddies field as well (Figure 5.1). The models do not produce enough low-frequency variability, which is evident from the contour levels in Figure 5.1, which shows the temporal variance of the 10-90 day eddies. They underestimate the variability by as much as 50% (e.g. in the Pacific variance maximum). The diminished magnitude is not a result of ensemble averaging in this case. For the calculation of the filtered data, the anomalies were calculated for each ensemble member, day, and year. The variance is then computed over the 90 day period and only then averaged over the ensemble members. The average is then computed over all 32 years to obtain the average position and amplitude of all features visible on the above maps. This indicates that either the pressure systems present tend to linger, whereas in reality they may have moved on, or that the amplitude of pressure systems is

underestimated. Either way, the models do not capture the realistic low-frequency variations of the 500 hPa geopotential height field.

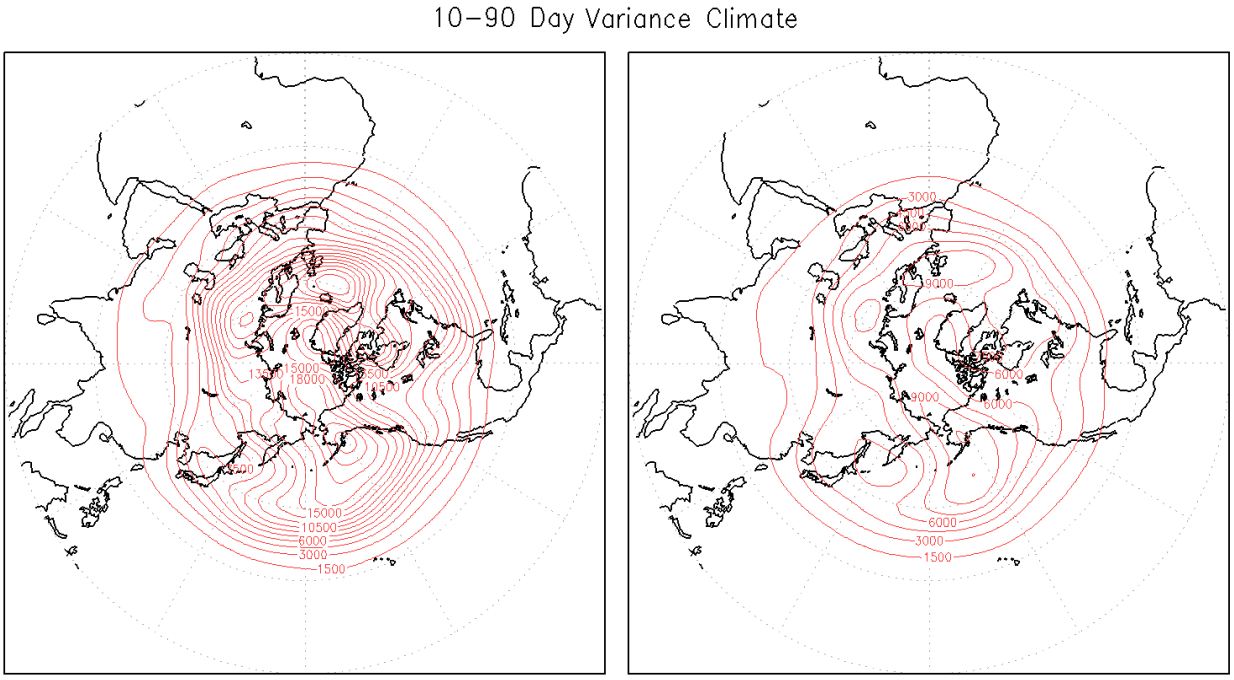

Figure 5.1: 32-year averaged 10-90 day variance of the 500 hPa geopotential height for (left) NCEP, (right) Multi-Model. The contour interval is 1500m^2.

Since the models underestimate the variance by such a large amount, a direct comparison becomes difficult; therefore the following plots of the variance climate (for all the following sections) will be normalized by the maximum value on the map (Figure 5.2). While these two plots are similar, the Pacific variance maximum is relatively too strong and extends slightly too far south, and the maximum located south of Iceland is shifted to the southeast of its reanalysis location, consistent with the bias observed in Chapter 3. Not only are these two centres associated with the PNA and NAO respectively, but they play pivotal roles in the occurrences of blocking events. When the PNA (NAO) is in its negative phase, blocking events occur up to

100% more often in the central North Pacific (northwest Atlantic) (Croci-Maspoli et al. 2007). The locations of blocking events are consistent with the low-frequency maximum variance centres located over the Aleutian Islands and Iceland. These low-frequency variations are due to a combination of planetary- and synoptic-scale waves (Blackmon 1976). Any misrepresentation of the low-frequency eddies will therefore affect the location of the synoptic transients. This highlights the importance of correctly representing these low-frequency atmospheric waves, given that they affect the representation of synoptic weather events. The variance minimum over the Rocky Mountains is again in the correct location although at a relatively larger magnitude than the reanalysis. The location of the maximum variance also differs between the reanalysis and model maps. The reanalysis data has its maximum low-frequency variance just south of Iceland (60N,20W), whereas the models have their maximum off the southern coast of Alaska (60N,155W). This may be a potential cause of the degradation of the NAO skill. Its centre of maximum variability is poorly represented in both location and relative intensity, meaning that the loading pattern used to compute the index is not covering the centre associated with the NAO in the models. In fact this location represents the only region where the models *relatively* underestimate the low-frequency variance.

The forecast skill for both the DJF 500 hPa height and the near-surface air temperature display significant skill in similar regions (Figure 5.3). The 500 hPa heights and near-surface air temperature west of the Aleutian Islands display appreciable skill when compared to the reanalysis data. There is also some skill is the area south of Iceland associated with the low-frequency variance maximum in the multi-model average. The skill observed for the near-surface air temperature is not particularly noteworthy. The majority of the skill is located over the oceans, where the temperature varies much more slowly in response to slowly varying SSTs. The

low-frequency component of the near-surface air temperature tends to have a much higher standard deviation over northern land masses (Blackmon et al. 1977). The high correlation over the oceans is therefore partly due to the slowly varying anomalies over the oceans, in contrast to more rapidly varying anomalies over land surfaces. The centres of high correlation over the Aleutian Islands, western North America, and the Gulf of Mexico are roughly collocated with the pressure centres associated with the PNA (Figure 1.1). The high correlation over Greenland and in the Atlantic to the north- and south-west of Portugal may be associated with the NAO although these centres are more removed than those associated with the PNA. The low-frequency temperature variations lend further credence to the hypothesis that the teleconnection patterns lend their skill to this component of variability (Figure 5.3). Even though the standard deviation is quite low over the oceans (not shown), the locations of high correlation do coincide with locations of temperature anomalies associated with each the PNA and NAO (refer to Figures 4.2 and 4.7; top respectively). The area of high correlation over the Pacific is consistent with the location of a pressure system centred over the Aleutian Islands. A low (high) in this area would bring warm (cold) air from the south (north) into the region. The high correlation off the coast of Brazil is also consistent with the temperature pattern forced by the NAO (refer to Figure 4.10).

Other variables such as the outgoing longwave radiation (OLR) and precipitation rate display much less skill; however this is not unexpected since the precipitation rate is a difficult quantity to predict, and the OLR is strongly related to convective systems, and thus would not have a strong low-frequency presence outside of the tropics.

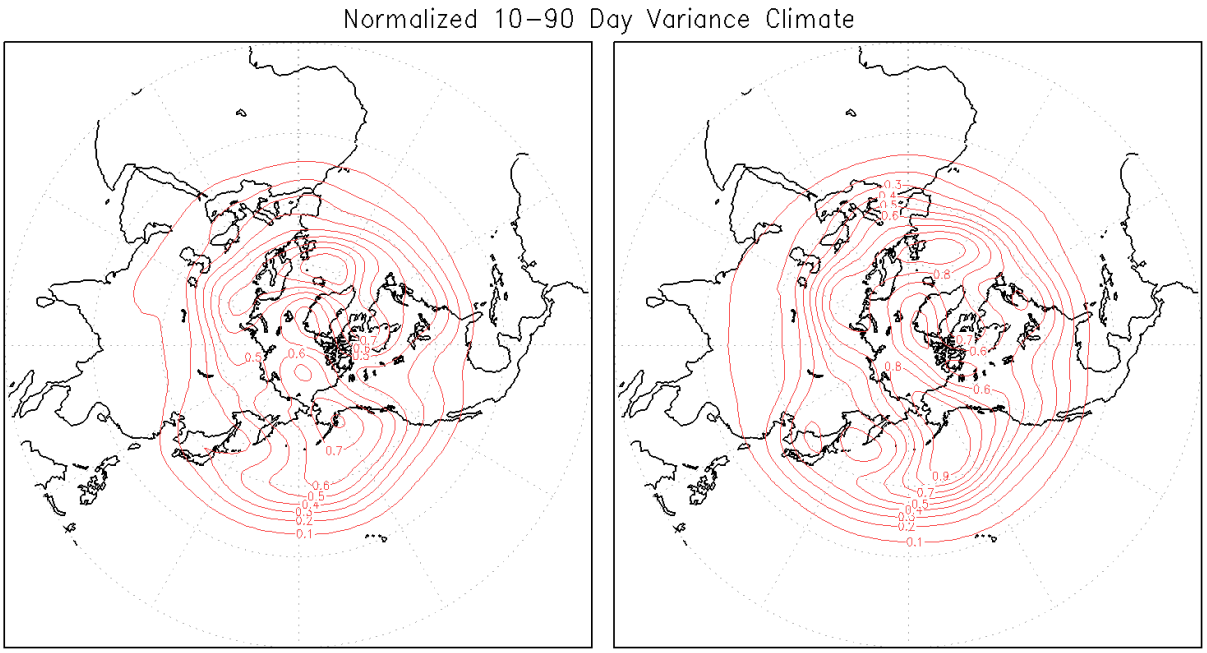

Figure 5.2: As is Figure 5.1 but normalized by the maximum value on the map. Maximum values are (left) NCEP: 26817m2, and (right) Multi-Model: 10592.5m2.

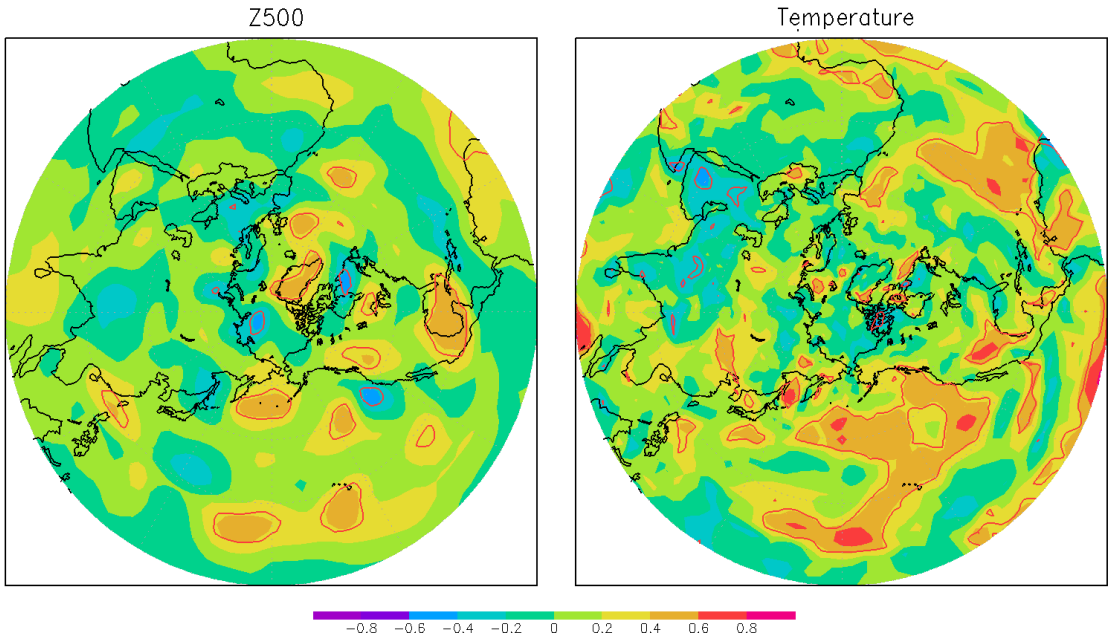

Figure 5.3: Low-frequency (left) 500 hPa geopotential height, and (right) 2m air temperature forecast skill for one-month lead DJF forecast.

5.2 Representation of the Synoptic Transients

The slowly-varying climate patterns and low-frequency eddies determine the location and intensity of the high-frequency features. There have been many studies documenting the relationship between the large-scale mean flow and storm tracks (e.g. Hurrell 1995; Lau 1988; Rogers 1990). The teleconnection patterns discussed previously impact the location and intensity of the storm track in their respective basins (Lau 1988). Therefore we expect that the ability of the models to accurately forecast the location and intensity of the teleconnection patterns will be inherited by these flow patterns. Furthermore the differences between the reanalysis and multi-model seasonally averaged flow will again affect how these same models represent the synoptic transients. The centres of maximum 2-9 day variability occur to the southeast of the standing troughs, and then terminate at the location of the standing ridges (Figure 5.4). These maxima are primarily generated by synoptic (spatial) scale waves, while the smaller maximum located over Russia is mainly generated by smaller scale waves with minor contributions from the synoptic scale waves (Blackmon 1976). The maximum over Russia is not an area of high storm occurrence, genesis, or lysis (Sickmoller et al. 2000). The average variance of the 2-9 day transients is underestimated by around 50%, as was the case with the low-frequency eddies. *Relatively* speaking, the intensity of the Atlantic storm track is well represented although it is shifted slightly south (Figure 5.5). The bias presented in Figure 5.5 is the normalized reanalysis field subtracted from the multi-model field. The Pacific storm track contains too much variability *relative* to the Atlantic storm track and its reanalysis counterpart. The models also *relatively* underestimate the intensity of the variance maximum over Russia.

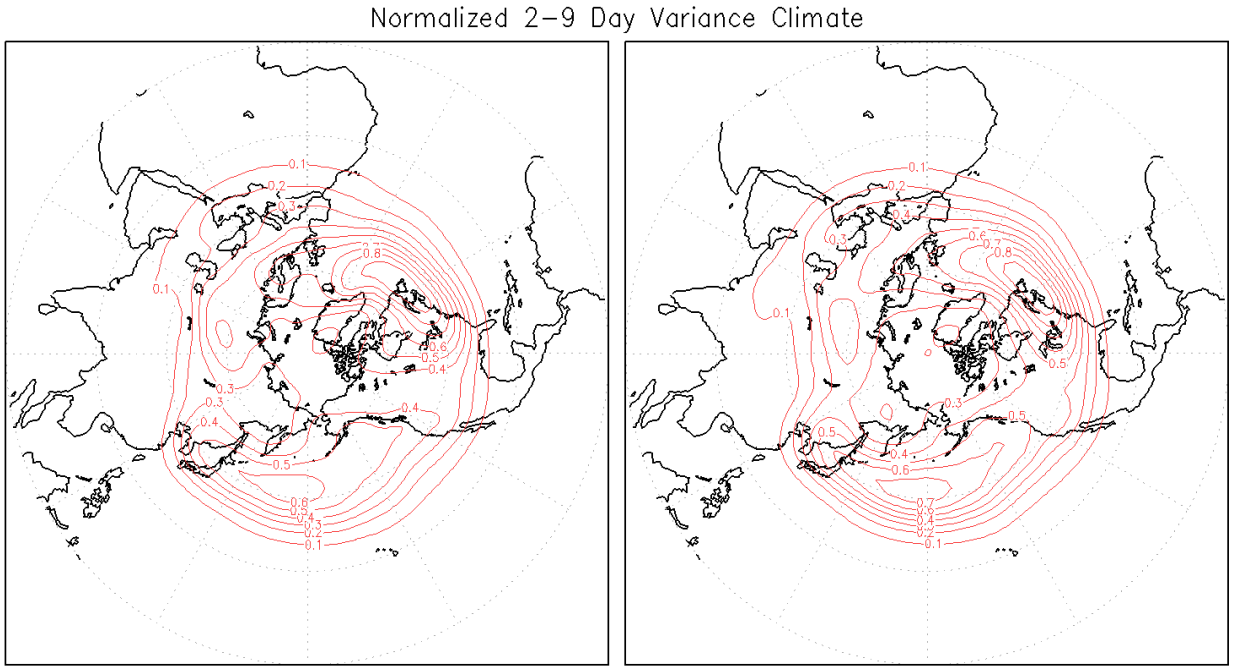

Figure 5.4: 32 year average of two-nine day variance normalized by the maximum value on the map. (left) NCEP, maximum value 8478.15m2; (right) multi-model, maximum value 4420.91m2.

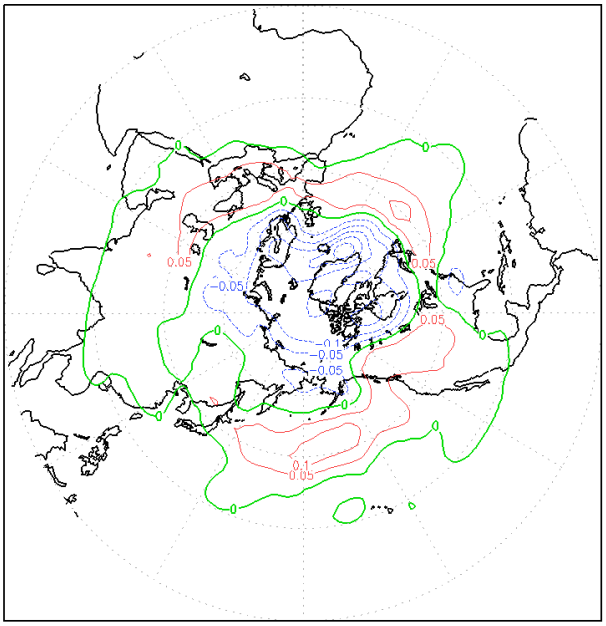

Figure 5.5: Difference map between multi-model and NCEP normalized 32 year average of two-nine day variance.

The position and intensity of the storm tracks vary with the Northern Hemisphere teleconnection patterns (Grise et al. 2013). The positive phase of the NAO is characterized by an increase in variance over northwestern Europe extending to the Caspian Sea, consistent with a north eastward shift of the Atlantic storm track (Hurrell et al. 2003; Rogers 1990). This pattern can be reproduced by taking the correlation of the two-nine day seasonal variance with the DJF NAO index (Figure 5.6; top). There is also a mild decrease in variance off the coast of Portugal (Figure 5.6; top left panel) associated with the positive phase of the NAO. This region is consistent with the negative phase of the NAO having a more zonal flow pattern than the positive phase. The negative phase of the NAO is marked by a correspondingly zonal storm track, and slightly increased storminess in the eastern Atlantic near 40^{o}N (Rogers 1990); hence the negative correlation.

The positive phase of the NAO is also marked by a stronger, more elongated jet stream (Wettstein and Wallace 2010), and thus increased variance in the vicinity of the Black and Caspian seas. The positive phase of the PNA is characterized by an equatorward shift of the storm track (Wettstein and Wallace 2010). The negative phase is therefore characterized by a pole-ward shift relative to climatology, and thus increased flow over the Rocky Mountains increasing the variance in their lee (Figure 5.6; middle). The pattern associated with ENSO is quite similar to that associated with the PNA. Given that a positive SST anomaly associate with an El-Nino event forces a Rossby wave train analogous in structure to the PNA (Horel and Wallace 1981), the similarity of their relationship to the two-nine day transients is expected. The models capture the broad patterns; however the majority of the maps in the right panels of Figure 5.6 resemble the correlation map associated with ENSO (Figure 5.6; bottom). This again supports the conclusion that ENSO's linear influence is much too prevalent within the models.

The correlation of each index (NAO, PNA, and Nino-3.4) with the two-nine day variance yields similar maps, with the centres of maximum correlation resembling those associated with ENSO (Figure 5.6). Over North America we can note similarities between the PNA and ENSO related variance anomalies. Most notably is the west coast of North America, which increases during the negative phase of both ENSO and the PNA.

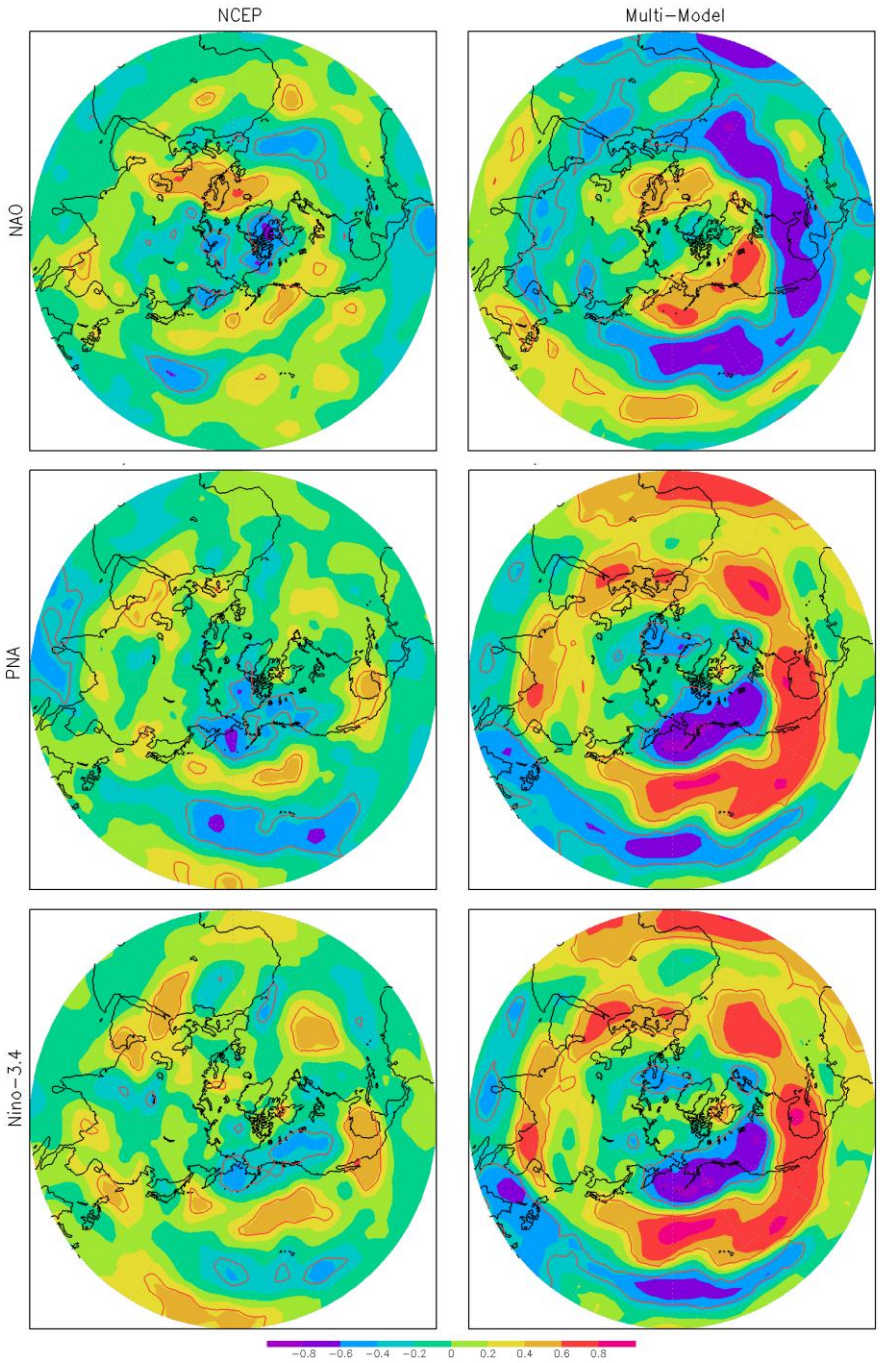

Figure 5.6: Correlation of two-nine day transients with (top) NAO, (middle) PNA, and (bottom) Nino-3.4 indices. Red contours denote regions passing the 95% significance level.

The synoptic transients over Western Europe and Scandinavia display a strong relationship to the NAO. These are also regions in which there are temperature anomalies that force the NAO (Figure 4.11). The area of high correlation within the models only covers Scandinavia, but does not extend south into Europe. Since the phase of the NAO contributes to the variability of temperature and moisture transport over this region (Hurrell 1995), the variability of near-surface air temperature and snow-depth may be misrepresented as well.

The one-month lead forecast skill for the two-nine day variance of the 500 hPa geopotential height, and near-surface air temperature display some similar features. In both cases there is little forecast skill in the storm track regions; however, in there is skill present in the area lee of the Rocky Mountains (Figure 5.7). This region is an important area of cyclogenesis for North America (Grise et al. 2013), and therefore predictions of extreme events (variance of two-nine day transient) in this area directly affect the forecasts downstream.

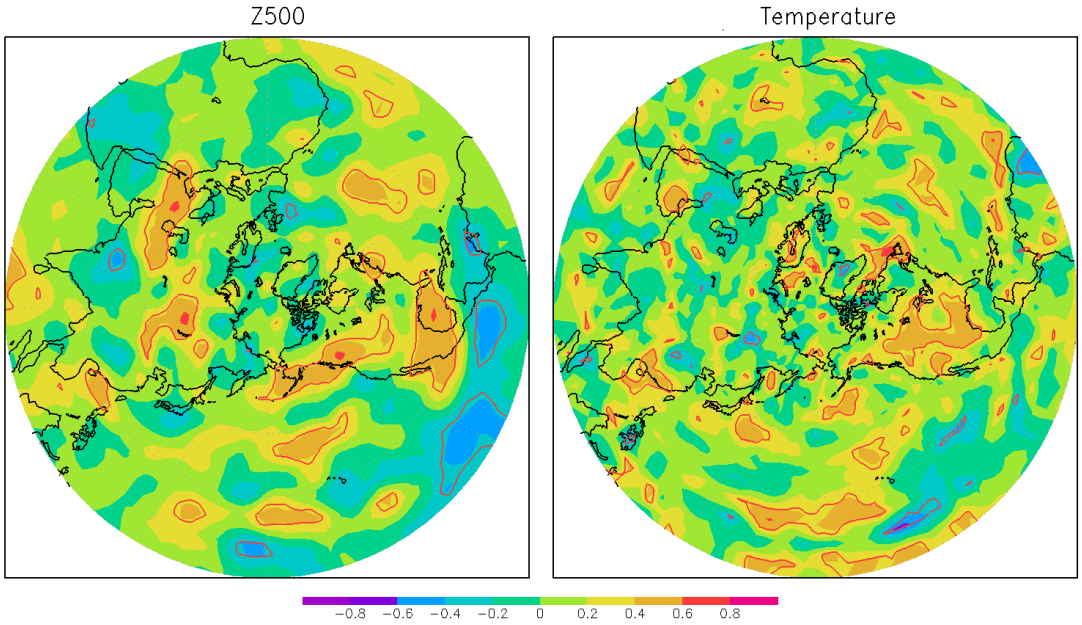

Figure 5.7: High-frequency (left) 500 hPa geopotential height, and (right) 2m air temperature forecast skill for the one-month lead DJF forecast.

5.3A Brief Comparison between the Fourier and Digital Filters

As mentioned in Chapter 2, the Fourier time filter is much more computationally expensive than the digital filter; however it also allows for a precise control over the cut-off frequency. The digital filter has a transition zone which contaminates the frequency band desired with some of the frequencies which are being filtered out. For this reason it is of interest to examine whether this frequency contamination has a noticeable and adverse effect, which offsets the convenience and simplicity of the digital filter. Note however, that in this section the high-frequency transients have a period range of two-10 days as opposed to two-nine days in the previous section. There is a decrease of variance in the high-frequency range (~36%) (Figure 5.8; compare to Figure 5.4), and an increase in the low-frequency range (~39%) (Figure 5.9; compare to Figure 5.1. This is the result of frequencies outside the desired range influencing the results. Using the digital filter, the models still reproduce only 50% of the total variance in both frequency ranges. In the low-frequency range the difference between the two methods manifests itself as a displacement of the Pacific centre to the East (Figure 5.10). The largest difference between the reanalysis and multi-model average still lies in the Atlantic, with the southeastward shift of the variance maximum. In the high-frequency portion, the main difference between the two methods is the relative increase of the bias in the average intensity of the Atlantic storm track (Figure 5.11). Even with these slight differences in position and intensity, the correlation with the PNA, NAO, and Nino-3.4 indices yield no difference compared to the Fourier time filter (not shown).

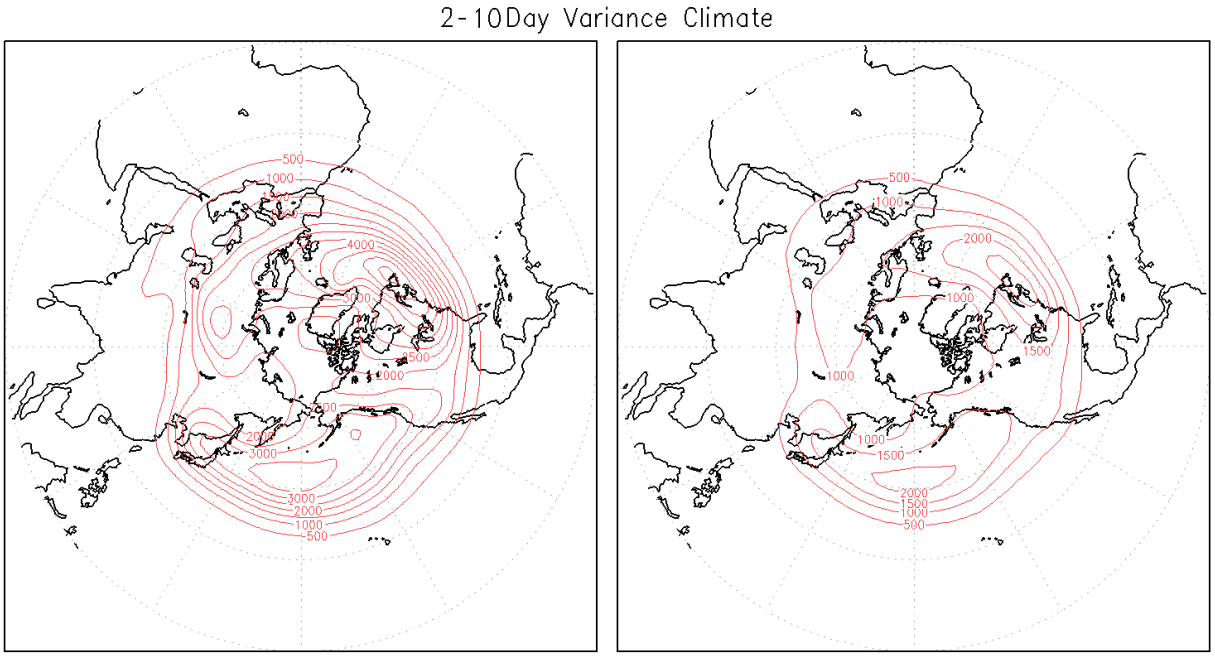

Figure 5.8: As in Figure 5.1 but for the digital filtered two-nine day variance climate. (Left) reanalysis, and (right) one-month lead multi-model average.

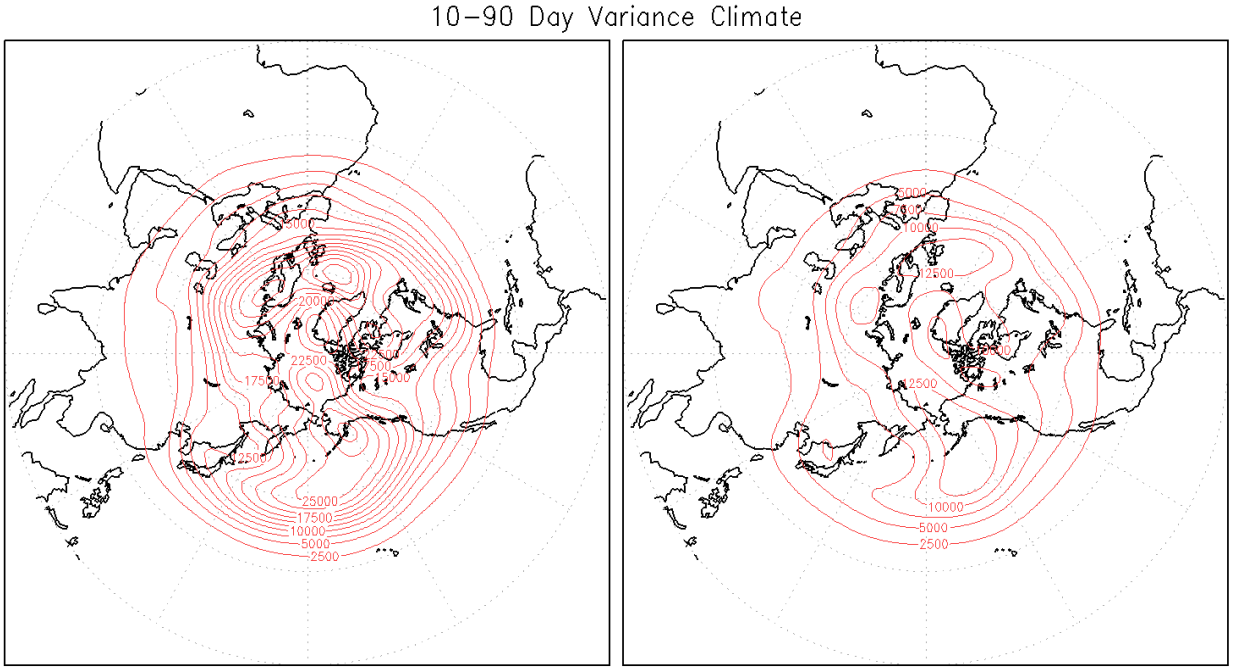

Figure 5.9: As in Figure 5.1, but for the digital filtered data.

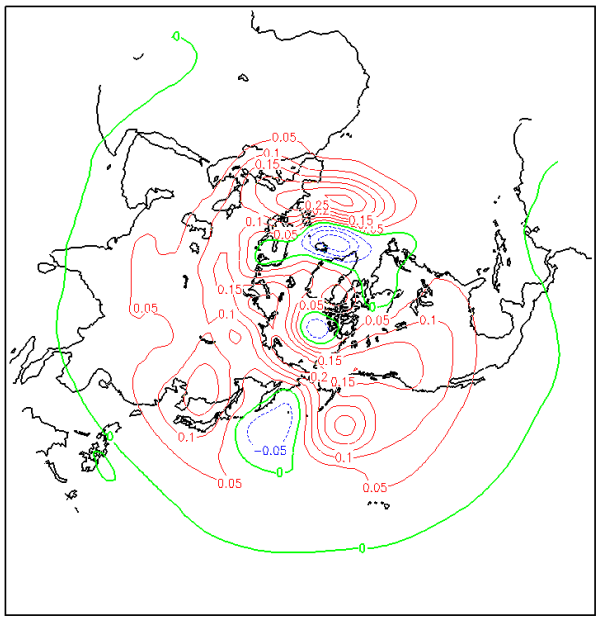

Figure 5.10: As in Figure 5.5 but for the digital filter 10-90 day eddies.

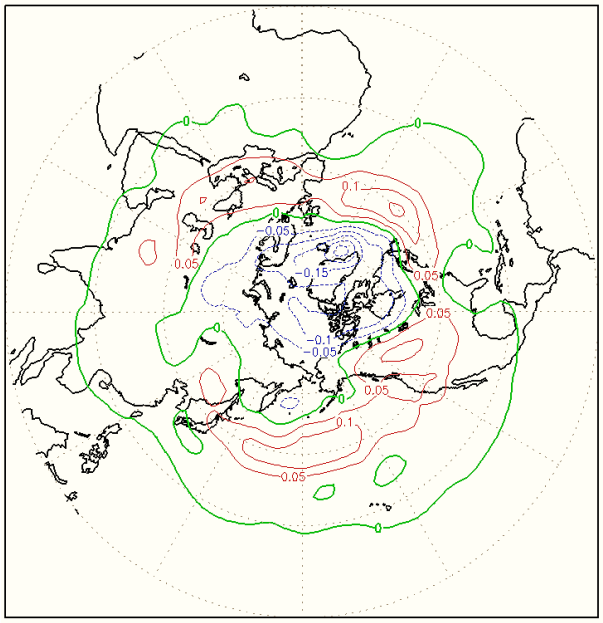

Figure 5.11: As in Figure 5.7 but for the synoptic transients.

Another, somewhat surprising, difference is the correlation of the multi-model 500 hPa geopotential heights with the reanalysis, yielding a significant relationship in the Indian Ocean, and in areas across the tropical Pacific Ocean (Figure 5.12) possibly related to the Madden-Julian Oscillation (MJO) (Madden and Julian 1972). This hypothesis needs further testing with variables more related to the MJO, such as zonal wind.

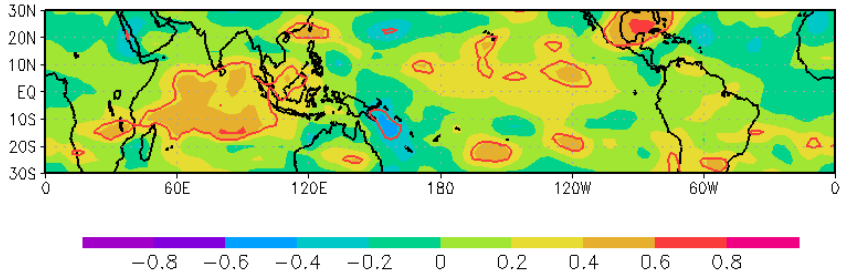

Figure 5.12: As in Figure 5.4 (left panel) for the Tropics, using the digital filter. Regions within the red contours pass the 95% significance level.

6 Conclusion

Using data from a pair of global atmosphere-ocean coupled models from the Canadian Seasonal to Interannual Prediction System (Merryfield et al. 2013) a comparison study was carried out to determine whether these models were able to capture variability associated with both the Pacific/North American pattern (PNA), and North Atlantic Oscillation (NAO). Furthermore, following the correction approach outlined by Lin et al. (2005) to statistically remove model bias and error, a Singular Value Decomposition (SVD) analysis (Bretherton et al. 1992) was used to correct the predicted 500 hPa geopotential height field. These corrected forecasts were used to inspect if any improvement could be gained in this fashion.

The models biases were found in the 500 hPa geopotential height field in locations consistent with the Northern hemisphere standing ridges and troughs (Blackmon 1976). These troughs are related with two of the dominant large scale flow patterns, the PNA and the NAO, which are both linked to the ocean basins (Horel and Wallace 1981; Czaja and Frankignoul 2002). The sea-surface temperature field displays very little bias and much more realistic inter-annual variations when compared to the 500 hPa geopotential height field, which exhibited much weaker inter-annual variability than that of the National Centers for Environmental Prediction/National Center for Atmospheric Research (NCEP/NCAR) reanalysis data. Therefore, the SVD patterns were used in an attempt to correct the 500 hPa geopotential height field over the entire Northern hemisphere. This technique modifies the model forecast by substituting SVD patterns from the reanalysis rather than the model patterns which may be erroneous.

Given the forecast skill level already present in forecasting the winter mean state, using a limited number of SVD patterns for the correction process was found to hold no benefit. The patterns derived from the model fields still provide interesting insight. The first pair of patterns accounts for over 90% of the total squared covariance, and help explain the pervasiveness of the ENSO signal in almost all model related figures. The strong ENSO signal and the model skill in forecasting the Tropical Pacific SST yield good PNA skill regardless of the lead time. The NAO predictions however only display appreciable skill out to the one-month lead forecast. The statistical correction process in fact lowered the forecast skill of these two teleconnection patterns.

The PNA has a well-documented relationship to ENSO (Horel and Wallace 1981; Mo et al. 1998), while the NAO is less influenced by forces external to the atmosphere (Hurrell et al. 2003); however, over the course of the last couple of decades there has been a rising interest in detecting sources of predictability for the NAO. The PNA has a very linear relationship to ENSO, where strong ENSO events generate a strong PNA event of the same sign. This relationship is strongest for extreme positive ENSO events, while the NAO is correlated to the non-extreme events (Derome et al. 2005). There is also evidence that the NAO is linked to negative ENSO events (Pozo-Vázquez et al. 2005), although this was barely discernable within the reanalysis data. The scatter plots for the relationship between the phase and amplitude of the NAO and ENSO seemed to hint at a possible quadratic relationship, whereby a strong positive or negative ENSO event forces a positive NAO pattern (Lin and Derome 2004; Wu and Hsieh 2004). This relationship was absent from the models, which displayed a strong negative correlation with ENSO. Moreover, the modelled NAO index has a higher correlation with positive ENSO events, which is contrary to both previous studies, and the pattern observed in the

reanalysis data. This seems to imply that internal dynamics plays an important role, especially during negative ENSO events. All of these results highlight the importance of internal variability in regards to the predictability of the NAO, and require further investigation.

Temperature anomalies in the Atlantic Ocean are part of a feedback loop involving the NAO (Czaja and Frankignoul 2002). The Atlantic tri-pole pattern evolves into the "horseshoe" pattern due to advection. This "horseshoe" pattern then modulates the strength of the NAO. To find these patterns, another SVD analysis was performed for the Northern Hemisphere geopotential height field and the Atlantic Ocean basin. The tri-pole pattern is immediately recognizable as the first SST SVD pattern associated with the NAO in both the reanalysis and the models. Upon regressing the first 500 hPa geopotential height PC onto the SST anomalies for subsequent and preceding seasons, the "horseshoe" pattern emerges in the reanalysis data for the preceding season. This "horseshoe" pattern is entirely missing from the model data preceding the NAO.

A similar lack of relationship was found between the Eurasian temperature and snow depth, and the NAO within the CanSIPS models. The reanalysis data shows a cold anomaly in Europe and a warm anomaly in China which precede the NAO by a month. The same pattern is observed when snow-depth precedes the NAO by a full season. Since snow-depth has a maximum in inter-annual variability during the fall, and is related to the temperature in the following season (Foster et al. 1983; Robinson et al. 1993), the correlation maps are nearly identical. Only small areas along the Himalayas, and a few patches in China are consistent between the models and the reanalysis fields. Finally, the area of correlation over Western Europe is missing from the models. This may suggest that one of the two NAO formation pathways described by Cohen et al. (2002) is not captured by the models, or that the Atlantic

storm track is poorly represented. The PNA has also been shown to have a predictability source overlying the Tibetan Plateau (Lin and Wu 2011), although this pattern was present in the models, it was not in the reanalysis data. Furthermore, the pattern of correlation between the November near-surface air temperature and the DJF PNA index shares features in common to that of the correlation plot involving the NAO. It is therefore impossible to say that this region represents a source of predictability for the PNA within these models.

To further understand the effects of the PNA and NAO on other atmospheric variables and flow features, the 500 hPa geopotential height field was decomposed in low-frequency eddies, and synoptic transients (10-90 day, and two-nine day periods, respectively), as was the near-surface air temperature. The multi-model average captures approximately 50% of the variance displayed in the reanalysis plots, which seems to indicate either that pressure systems are less frequent, or slower in the models, or that their intensity is weaker. For comparison we normalized all subsequent plots by the maximum value on the map to get an idea of the relative importance of the variance centres, and to verify if the models are distributing the variance correctly.

The 500 hPa geopotential height low-frequency eddies have two major centres of variability, one over the Aleutian Island, and one off the coast of Iceland. These variance centres are associated with the PNA and NAO respectively, and also contribute to blocking events over their ocean basins (Croci-Maspoli et al. 2007). Furthermore, the locations of these low-frequency eddies then affect where the storm tracks will occur. In the models the variance maximum over the Aleutian Islands is slightly too strong relative to the centre over Iceland, however its location is in good agreement with the reanalysis. The maximum over Iceland is displaced to the south and east of its reanalysis location. In terms of relative intensity, this variance maximum is the

only location where the models underestimate the variance. The forecast skill of the low-frequency temperature variations display an area of significant skill off the west coast of North America, consistent with the area of effect of the PNA; no such area is present in the North Atlantic. The area of significant skill off the coast of Brazil is consistent with the temperature pattern forced by the NAO. The forecast skill of the geopotential height field has an area of significant skill in locations congruent with the pressure centres of the PNA, whereas those associated with the NAO are further removed from the locations where the pressure systems should be.

The synoptic transients, which are too weak in the models, are much more consistent with their reanalysis counterpart both in terms of location and relative intensity; however, there are a few subtle differences which are visible only when the difference between the two is taken. The Pacific storm track is slightly too strong, while the Atlantic one is displaced slightly to the southeast, consistent with the bias observed in the low-frequency field. Their association with ENSO, the PNA, and the NAO differ much more. In the models the PNA and ENSO related correlation plots are nearly identical, with negative correlation over the Rocky Mountain, and positive correlation in the central east Pacific. These correlation maxima depict a southward shift of the Pacific storm track during a positive PNA event, while a negative PNA is characterized by a slight poleward shift increasing the flow over the Rocky Mountains (Wettstein and Wallace 2010). The negative phase of the NAO is characterized by increased storminess in the Eastern Atlantic near 40^{o}N, and a northeastward shift during it positive phase (Rogers 1990). The Atlantic storm track is also elongated during a positive NAO (Wettstein and Wallace 2010). This last feature is not present within the model correlation plots, which may help explain the lack of relationship between the November temperature and the winter NAO. All of the model plots

resemble that of the synoptic transients' association with ENSO (with an opposing sign for the NAO plot), again illustrating ENSO's dominance in terms of inter-annual variability.

The Fourier filter used to compute the temporally decomposed fields is quite computationally expensive. A digital filter, in which is applied as a weighted running mean, provides a much simpler alternative, with little noticeable change in any major feature. Furthermore, the correlation of the time filtered fields with the PNA, NAO and Nino-3.4 indices yielded no difference when compared to those using the Fourier filter. The only difference manifests itself as an increase in skill over the Indian Ocean in the low-frequency 500 hPa geopotential height field. This area is traditionally related to the Madden-Julian Oscillation (MJO) (Madden and Julian 1972); however, this result would need further testing with variables more related to the MJO, such as zonal wind, or outgoing longwave radiation.

This study shows that the CanSIPS models are able to accurately forecast the phase and amplitude of the PNA and ENSO for any lead time up to nine months. Conversely the variability related to the NAO is, in general, poorly captured and outlines the need for further study into this area. Given that the NAO is a key mode of atmospheric variability in the Northern Hemisphere (Barnston and Livezey 1987), but there is no strong link yet detect to any external forcing (Hurrell et al. 2003), any improvement in our understanding of its evolution, external forcing mechanism, or relationship to other teleconnection patterns has the potential to greatly improve the accuracy of forecasts of much of the Northern Hemisphere.

7 References

1. Bamzai, A.S., 2003. Relationship between snow cover variability and Arctic Oscillation Index on a hierarchy of time scales. *International Journal of Climatology*, 23(2), pp.131–142.

2. Barnston, A.G. and Livezey, R.E., 1987. Classification, Seasonality and Persistence of Low-Frequency Atmospheric Circulation Patterns. *Monthly Weather Review*, 115(6), pp.1083–1126.

3. Blackmon, M.L., 1976. A Climatological Spectral Study of the 500 mb Geopotential Height of the Northern Hemisphere. *Journal of the Atmospheric Sciences*, 33(8), pp.1607–1623.

4. Blackmon, M.L., Wallace, J.M., Lau, N.-C., and Mullen, S.L., 1977. An Observational Study of the Northern Hemisphere Wintertime Circulation. *Journal of the Atmospheric Sciences*, 34(7), pp.1040–1053.

5. Bretherton, C.S., Smith, C. and Wallace, J.M., 1992. An Intercomparison of Methods for Finding Coupled Patterns in Climate Data. *Journal of Climate*, 5(6), pp.541–560.

6. Cohen, J. and Entekhabi, D., 1999. Eurasian snow cover variability and northern hemisphere climate predictability. *Geophysical Research Letters*, 26(3), pp.345–348.

7. Cohen, J., Saito, K. and Entekhabi, D., 2001. The role of the Siberian high in Northern Hemisphere climate variability. *Geophysical Research Letters*, 28(2), pp.299–302.

8. Cohen, J., Salstein, D. and Saito, K., 2002. A dynamical framework to understand and predict the major Northern Hemisphere mode. *Geophysical Research Letters*, 29(10), pp.51–1 – 51–4.

9. Croci-Maspoli, M., Schwierz, C. and Davies, H.C., 2007. Atmospheric blocking: space-time links to the NAO and PNA. *Climate Dynamics*, 29(7-8), pp.713–725.

10. Czaja, A. and Frankignoul, C., 2002. Observed Impact of Atlantic SST Anomalies on the North Atlantic Oscillation. *Journal of Climate*, 15, pp.606–623.

11. Derome, J., Brunet, G., Plante, A., Gagnon, N., Boer, G. J., Zwiers, F. W., Sheng, J., and Ritchie, H., 2001. Seasonal predictions based on two dynamical models. *Atmosphere-Ocean*, 39(4), pp.485–501.

12. Derome, J., Lin, H. and Brunet, G., 2005. Seasonal Forecasting with a Simple General Circulation Model : Predictive Skill in the AO and PNA. *Journal of Climate*, 18(4), pp.597–609.

13. Feddersen, H., Navarra, A. and Ward, M.N., 1999. Reduction of Model Systematic Error by Statistical Correction for Dynamical Seasonal Predictions. *Journal of Climate*, 12(7), pp.1974–1989.

14. Foster, J., Owe, M. and Rango, A., 1983. Snow Cover and Temperature Relationships in North America and Eurasia. *Journal of Climate and Applied Meteorology*, 22(3), pp.460–469.

15. Gong, D.-Y., Wang, S.-W. and Zhu, J.-H., 2001. East Asian Winter Monsoon and Arctic Oscillation. *Geophysical Research Letters*, 28(10), pp.2073–2076.

16. Gong, G. and Entekhabi, D., 2003. Relative impacts of Siberian and North American snow anomalies on the winter Arctic Oscillation. *Geophysical Research Letters*, 30(16), pp.1848–1851.

17. Gong, G., Entekhabi, D. and Cohen, J., 2003. Modeled Northern Hemisphere Winter Climate Response to Realistic Siberian Snow Anomalies. *Journal of Climate*, 16(23), pp.3917–3931.

18. Greatbatch, R.J., Lin, H., Lu, J., Peterson, A., and Derome, J., 2003. Tropical/Extratropical forcing of the AO/NAO: A corrigendum. *Geophysical Research Letters*, 30(14), p.1738.

19. Grise, K.M., Son, S.-W. and Gyakum, J.R., 2013. Intraseasonal and Interannual Variability in North American Storm Tracks and Its Relationship to Equatorial Pacific Variability. *Monthly Weather Review*, 141(10), pp.3610–3625.

20. Hamming, R.W., 1989. *Digital Filters* 3rd ed., Englewood Cliffs: Prentice-Hall.

21. Horel, J.D. and Wallace, J.M., 1981. Planetary-Scale Atmospheric Phenomena Associated with the Southern Oscillation. *Monthly Weather Review*, 109(4), pp.813–829.

22. Hoskins, B.J., James, I.N. and White, G.H., 1983. The Shape, Propagation and Mean-Flow Interaction of Large-Scale Weather Systems. *Journal of the Atmospheric Sciences*, 40(7), pp.1595–1612.

23. Hurrell, J.W., Kushnir, Y., Ottersen, J., and Visbeck, M., 2003. An Overview of the North Atlantic Oscillation. In J. W. Hurrell et al., eds. *The North Atlantic Oscillation: Climatic Significance and Environmental Impact*. Washington D.C.: American Geophysical Union, pp. 1–35.

24. Hurrell, J.W., 1995. Decadal trends in the north atlantic oscillation: regional temperatures and precipitation. *Science (New York, N.Y.)*, 269(5224), pp.676–9.

25. Jia, X., Lin, H. and Yao, X., 2014. The Influence of Tropical Pacific SST Anomaly on Surface Air Temperature in China. *Journal of Climate*, 27(4), pp.1425–1444.

26. Kalnay, E., Kanamitsu, M., Kistler, R., Collins, W., Deaven, D., Gandin, L., Iredell, M., Saha, S., White, G., Woollen, J., Zhu, Y., Leetmaa, A., Reynolds, R., Chelliah, M., Ebisuzaki, W., Higgins, W., Janowiak, J., Mo, K. C., Ropelewski, C., Wang, J., Jenne, Roy., and Joseph, D., 1996. The NCEP/NCAR 40-Year Reanalysis Project. *Bulletin of the American Meteorological Society*, 77(3), pp.437–471.

27. Kumar, A., Hoerling, M. P., Ji, M., Leetmaa, A., and Sardeshmukh, P., 1996. Assessing a GCM's Suitability for Making Seasonal Predictions. *Journal of Climate*, 9(1), pp.115–129.

28. Latif, M., Barnett, T. P.,Cane, M. A., Flugel, M., Graham, N. E., Von Storch, H., Xu, J.-S., and Zebiak, S. E., 1994. A review of ENSO prediction studies. *Climate Dynamics*, 9(4-5), pp.167–179.

29. Lau, N.-C., 1988. Variability of the Observed Midlatitude Storm Tracks in Relation to Low-Frequency Changes in the Circulation Pattern. *Journal of the Atmospheric Sciences*, 45(19), pp.2718–2743.

30. Lin, H., Derome, J., Greatbatch, R. J., Peterson, A., and Lu, J., 2002. Tropical links of the Arctic Oscillation. *Geophysical Research Letters*, 29(20), p.1943.

31. Lin, H. and Derome, J., 2004. Nonlinearity of the Extratropical Response to Tropical Forcing. *Journal of Climate*, 17(13), pp.2597–2608.

32. Lin, H. and Derome, J., 2003. The atmospheric response to North Atlantic SST. *Tellus*, 55A, pp.193–207.

33. Lin, H., Derome, J. and Brunet, G., 2005. Correction of atmospheric dynamical seasonal forecasts using the leading ocean-forced spatial patterns. *Geophysical Research Letters*, 32(14), p.L14804.

34. Lin, H. and Wu, Z., 2011. Contribution of the Autumn Tibetan Plateau Snow Cover to Seasonal Prediction of North American Winter Temperature. *Journal of Climate*, 24(11), pp.2801–2813.

35. Van Loon, H. and Rogers, J.C., 1978. The Seesaw in Winter Temperatures between Greenland and Northern Europe. Part I: General Description. *Monthly Weather Review*, 106(3), pp.296–310.

36. Lorenz, E.N., 1969. The predictability of a flow which possesses many scales of motion. *Tellus*, 21(3), pp.289–307.

37. Madden, R.A. and Julian, P.R., 1972. Description of Global-Scale Circulation Cells in the Tropics with a 40-50 Day Period. *Journal of the Atmospheric Sciences*, 29(6), pp.1109–1123.

38. Merryfield, W.J., Lee, W.-S., Boer, G. J., Kharin, Viatcheslav V., Scinocca, J. F., Flato, G. M., Ajayamohan, R. S., Fyfe, J. C., Tang, Y., and Polavarapu, S., 2013. The Canadian Seasonal to Interannual Prediction System. Part I: Models and Initialization. *Monthly Weather Review*, 141(8), pp.2910–2945.

39. Mo, R., Fyfe, J. and Derome, J., 1998. Phase-locked and asymmetric correlations of the wintertime atmospheric patterns with the ENSO. *Atmosphere-Ocean*, 36(3), pp.213–239.

40. Murphy, J.M., 1988. The impact of ensemble forecasts on predictability. *Quarterly Journal of the Royal Meteorological Society*, 114, pp.463–493.

41. Climate Prediction Center Internet Team, 2005. North Atlantic Oscillation (NAO), image, viewed May 10th 2014. http://www.cpc.ncep.noaa.gov/data/teledoc/nao_map.shtml>

42. Climate Prediction Center Internet Team, 2005. Pacific/North American (PNA), image, viewed May 10th 2014. http://www.cpc.ncep.noaa.gov/data/teledoc/pna_map.shtml>

43. Peng, S., Robinson, W. a. and Li, S., 2003. Mechanisms for the NAO Responses to the North Atlantic SST Tripole. *Journal of Climate*, 16(12), pp.1987–2004.

44. Pozo-Vázquez, D. et al., 2005. North Atlantic Winter SLP Anomalies Based on the Autumn ENSO State. *Journal of Climate*, 18(1), pp.97–103.

45. Robertson, A.W., 2001. Influence of Ocean – Atmosphere Interaction on the Arctic Oscillation in Two General Circulation Models. *Journal of Climate*, 14, pp.3240–3254.

46. Robinson, D.A., Dewey, K.F. and Heim, R.R.J., 1993. Global Snow Cover Monitoring: An Update. *Bulletin of the American Meteorological Society*, 74(9), pp.1689–1696.

47. Rogers, J.C., 1990. Patterns of Low-Frequency Monthly Sea Level Pressure Variability (1899-1986) and Associated Wave Cyclone Frequencies. *Journal of Climate*, 3(12), pp.1364–1379.

48. Rogers, J.C. and van Loon, H., 1979. The Seesaw in Winter Temperatures between Greenland and Northern Europe. Part II: Some Oceanic and Atmospheric Effects in Middle and High Latitudes. *Monthly Weather Review*, 107(5), pp.509–519.

49. Saito, K., Cohen, J. and Entekhabi, D., 2001. Evolution of Atmospheric Response to Early-Season Eurasian Snow Cover Anomalies. *Monthly Weather Review*, 129(11), pp.2746–2760.

50. Seager, R. et al., 2010. Northern Hemisphere winter snow anomalies: ENSO, NAO and the winter of 2009/10. *Geophysical Research Letters*, 37(14), p.L14703.

51. Shukla, J., 1981. Dynamical Predictability of Monthly Means. *Journal of the Atmospheric Sciences*, 38(12), pp.2547–2572.

52. Sickmoller, M., Blender, R. and Fraedrich, K., 2000. Observed winter cyclone tracks in the northern hemisphere in re-analysed ECMWF data. *Quarterly Journal of the Royal Meteorological Society*, 126(563), pp.591–620.

53. Wallace, J.M. and Gutzler, D.S., 1981. Teleconnections in the Geopotential Height Field during the Northern Hemisphere Winter. *Monthly Weather Review*, 109(4), pp.784–812.

54. Wettstein, J.J. and Wallace, J.M., 2010. Observed Patterns of Month-to-Month Storm-Track Variability and Their Relationship to the Background Flow*. *Journal of the Atmospheric Sciences*, 67(5), pp.1420–1437.

55. Wu, A. and Hsieh, H.M., 2004. The nonlinear Northern Hemisphere winter atmospheric response to ENSO. *Geophysical Research Letters*, 31(2), p.L02203.

56. Wu, Q., Hu, H. and Zhang, L., 2011. Observed Influences of Autumn–Early Winter Eurasian Snow Cover Anomalies on the Hemispheric PNA-like Variability in Winter. *Journal of Climate*, 24(7), pp.2017–2023.